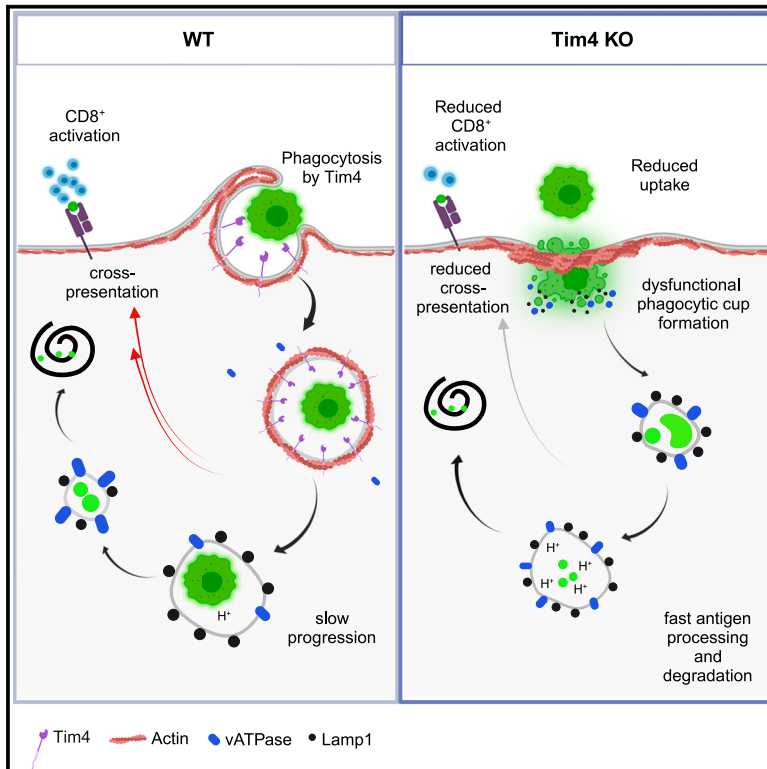


Tim4 enables large peritoneal macrophages to cross-present tumor antigens at early stages of tumorigenesis

Graphical abstract



Authors

Sonal Joshi, Lucía López,
Luciano Gastón Morosi, ...,
Giulia Maria Piperno, Daan Vorselen,
Federica Benvenuti

Correspondence

benvenut@icgeb.org

In brief

TIM4 orchestrates the processing of engulfed tumor antigens for cross-presentation by large peritoneal macrophages (LPMs). Joshi et al. reveal that TIM4-driven actin nucleation on nascent phagosomes delays phagolysosomal fusion, preventing rapid antigen destruction. By this mechanism, TIM4⁺ LPMs induce anti-tumoral responses at early stages of peritoneal invasion by ovarian cancer cells.

Highlights

- TIM4⁺ LPMs efficiently capture cancer cells in the peritoneal cavity
- TIM4-mediated uptake induces specific transcriptional remodeling in LPMs
- TIM4 directs slow progression of phagosomes, preserving antigens for cross-presentation
- TIM4-mediated cross-presentation induces anti-tumoral CD8 responses at tumor inception



Article

Tim4 enables large peritoneal macrophages to cross-present tumor antigens at early stages of tumorigenesis

Sonal Joshi,¹ Lucía López,¹ Luciano Gastón Morosi,¹ Roberto Amadio,¹ Manendra Pachauri,² Marco Bestagno,¹ Ironya Paul Ogar,^{1,3} Mauro Giacca,^{2,4} Giulia Maria Piperno,¹ Daan Vorselen,⁵ and Federica Benvenuti^{1,6,*}

¹Cellular Immunology, International Center for Genetic Engineering and Biotechnology (ICGEB), Trieste, Italy

²Department of Medical, Surgical, and Health Sciences, University of Trieste and International Center for Genetic Engineering and Biotechnology (ICGEB), Trieste, Italy

³Department of Biochemistry, Faculty of Basic Medical Sciences, College of Medical Sciences, University of Calabar, P.M.B. 1115 Calabar, Cross River State, Nigeria

⁴King's College London, British Heart Foundation Center of Research Excellence, School of Cardiovascular Medicine & Sciences, London, UK

⁵Department of Cell Biology & Immunology, Wageningen University & Research, 6708 PD Wageningen, the Netherlands

⁶Lead contact

*Correspondence: benvenuti@icgeb.org

<https://doi.org/10.1016/j.celrep.2024.114096>

SUMMARY

Receptors controlling the cross-presentation of tumor antigens by macrophage subsets in cancer tissues are poorly explored. Here, we show that TIM4⁺ large peritoneal macrophages efficiently capture and cross-present tumor-associated antigens at early stages of peritoneal infiltration by ovarian cancer cells. The phosphatidylserine (PS) receptor TIM4 promotes maximal uptake of dead cells or PS-coated artificial targets and triggers inflammatory and metabolic gene programs in combination with cytoskeletal remodeling and upregulation of transcriptional signatures related to antigen processing. At the cellular level, TIM4-mediated engulfment induces nucleation of F-actin around nascent phagosomes, delaying the recruitment of vacuolar ATPase, acidification, and cargo degradation. *In vivo*, TIM4 deletion blunts induction of early anti-tumoral effector CD8 T cells and accelerates the progression of ovarian tumors. We conclude that TIM4-mediated uptake drives the formation of specialized phagosomes that prolong the integrity of ingested antigens and facilitate cross-presentation, contributing to immune surveillance of the peritoneum.

INTRODUCTION

Tumor-associated macrophages (TAMs) include tissue-resident cells that exist prior to tumor development and monocyte-derived macrophages that differentiate *in situ* under tumor-derived cues. While a large body of evidence has established the tumor-promoting functions of monocyte-derived TAMs,^{1–5} the precise function of tissue-resident macrophages (TRMs) during initiation of primary tumors or early colonization of metastatic sites is still poorly understood. Sparse evidence suggests that, within TRMs, subsets with tumor-promoting functions^{6,7} coexist with subsets endowed with CD8 stimulatory properties.^{8,9} These data indicate that at least a fraction of TRMs possess intrinsic tumor-protective functions, depending on tumor tissue and stage, highlighting the importance of elucidating their function and therapeutic potential.

Cross-presentation, the specialized pathway to process and present exogenous tumor antigens on class-I major histocompatibility complex (MHC-I), is particularly efficient in conventional type I dendritic cells (cDC1s), a specialized subset invariably

linked to anti-tumorigenic properties via activation of anti-tumoral CD8 T cells.^{10,11} Cross-presentation, albeit less efficient on a per-cell basis,¹² can operate as well in monocyte-derived macrophages,^{13,14} and it is emerging as a critical factor to establish CD8 T cell exhaustion in advanced tumors.^{15,16} Conversely, the role, underlying mechanisms, and overall impact of cross-presentation by TRMs at initial tumor stages remain poorly explored.

The peritoneal cavity, the site of metastasis of gut and ovarian tumors, is dominated by two well-characterized classes of macrophages.¹⁷ Small peritoneal macrophages (SPMs) arise from bone marrow myeloid precursors, are poorly represented at steady state, and expand dramatically during inflammation and tumor progression. Large peritoneal macrophages (LPMs) are the largest population at steady state and derive from embryonic precursors, yet they can be replenished by long-lived bone marrow cells under Gata6-dependent environmental signals.^{18,19} While LPM intrinsic functions are linked to tissue repair, the subset acquires pro-tumorigenic functions during tumor progression, shifting to high production of reactive oxygen species



and autophagic adaptation.^{20–22} LPMs, like resident macrophages of the liver, spleen, and brain, express high levels of the phosphatidylserine (PS) receptor TIM4, which confers the ability to engulf apoptotic cells, contributing to silent clearance and maintenance of tissue homeostasis.^{23,24} In addition, TIM4 was recently found to regulate cholesterol metabolism in adipose tissue macrophages and during anti-viral responses.^{25,26} In cancer tissues, TIM4 has been associated with disparate, context-dependent functions. Cavity macrophages in advanced metastatic tumors use TIM4 to sequester PS-expressing, activated CD8⁺ T cells, dampening anti-tumoral responses.²⁷ Past work suggested that monocytes-derived TAMs infiltrating B16 subcutaneous tumors acquire TIM4 expression, which regulates autophagy and degradation of tumor antigens.²⁸ Conversely, our group previously uncovered that high expression of TIM4 by lung tissue-resident cDC1s in nascent tumors is required to engulf dying cancer cells and cross-present tumor antigens to initiate anti-tumoral T cell responses.²⁹ Human data confirmed that myeloid cells expressing TIM4 in tertiary lymphoid structures positively correlate to better survival across different cancer types.^{9,29} On these bases, we hypothesized that high levels of TIM4 on LPMs may contribute to scrutiny of antigenic content in incoming metastatic cells. By establishing a metastatic model of ovarian cancer expressing a phagocytic reporter and a model antigen, we show that, at initial tumor stages, TIM4 mediates uptake and cross-presentation of tumor antigens, leading to priming of peritoneal CD8⁺ T cells. Mechanistically, we uncover that TIM4 controls the trafficking of ingested dead cells, routing the cargo to cross-presentation-competent phagosomes.

RESULTS

Uptake of tumor cells is performed by TIM4-expressing LPMs in the peritoneal cavity

To investigate the role of TIM4 on peritoneal resident macrophages, we established a murine model of ovarian cancer that recapitulates the spreading of cancer cells to the peritoneum, based on the syngeneic line ID8.³⁰ ID8 was genetically engineered to express the pH stable reporter ZsGreen and the ovalbumin (OVA) model antigen (ID8^{ZGO}) to allow tracking of phagocytosis and presentation of tumor antigens.³¹ Tumor cells were implanted in the peritoneum, and tissues were harvested 24 h or 15 days after challenge to examine peritoneal macrophages immediately after seeding and at initial engraftment. Flow cytometry analysis of the peritoneal immune infiltrate showed that LPMs and SPMs (defined as F4/80^{high} MHC class II^{low} and F4/80^{low} MHC class II^{high}, respectively) expand and accumulate after 15 days, in line with past reports^{22,32} (Figures 1A and 1B). In addition, we observed a slight induction in the proportion of inflammatory monocytes, neutrophils, and CD8⁺ T cells in tumor-challenged mice, paralleled by a reduction in B cells (Figures S1A and S1B). In line with previous reports, a large fraction of steady-state LPMs showed strong TIM4 expression, which slightly declined in tumor-challenged animals. Weak TIM4 expression was also present on cDC1s, whereas no expression was detected on the other peritoneal phagocytes, including SPMs (Figure 1C). We next examined the acquisition of the ZsGreen signal by peritoneal phagocytes as a measure

of cancer cell uptake. LPMs displayed the highest phagocytic capacity (70.18% ± 9.24%), followed by cDC2 (27.87% ± 5.01%). In contrast, SPM, Ly6C⁺ monocytes and neutrophils were weakly associated with the ZsGreen signal (Figures 1D and S1C). Within LPMs, the uptake was restricted to the TIM4⁺ fraction both at 24 h and at 15 days, suggesting a selective ability of this population to engulf tumor cells (Figures 1E; and S1E). As a control, we verified that cancer cells in the peritoneum express PS, the ligand of TIM4 (Figure S1D). Confocal imaging of LPMs sorted from ID8-challenged mice confirmed actual internalization of tumor cells by TIM4⁺ LPMs (Figure 1F). Apart from LPMs, other subsets of macrophages residing in the peritoneal cavity, such as in the mesothelium and omentum, have also been shown to play an important role during ovarian cancer progression. The omentum is a fatty tissue that is formed from folds of mesothelium and hosts resident TIM4⁺ macrophage.⁷ However, TIM4 expression is much weaker on omental CD64^{high} F4/80^{high} resident macrophages than on LPMs, and we found a further decrease in tumor-challenged animals. In addition, cancer cell uptake was associated with TIM4⁻ cells in this context (Figures S2A–S2C). We conclude that LPMs expressing high TIM4 are specialized in capturing cancer cells seeding to the peritoneal cavity.

TIM4⁺ LPMs in the peritoneal cavity efficiently cross-present tumor-associated antigen

To understand transcriptional programs induced by cancer cell engulfment, we isolated, by cell sorting, the fraction of LPMs that had taken up ZsGreen⁺ fluorescence, 24 h after ID8^{ZGO} peritoneal challenge. As a control, we used LPMs from naive animals, as the ZsGreen⁻ fraction may contain cells that already degraded cargo, confounding the analysis. Bulk RNA sequencing (RNA-seq) revealed significant changes and differentially expressed genes induced by cancer cell uptake (Figures 2A and S3A; Table S1). Gene set enrichment showed prominent enrichment of inflammatory responses in LPMs that had engulfed cancer cells, in line with individual differentially expressed genes (DEGs) (Figures 2B and S3A). Moreover, cancer cell uptake induced metabolic rewiring of LPMs, increasing glycolysis and cellular respiration. Interestingly, pathways related to the degradation of ingested antigens and MHC class I antigen presentation were also enriched in LPMs loaded with cancer cells (Figure 2B). Based on these results, we moved to examine the cross-presentation of tumor antigens. Labeling with an antibody specific for the pMHC class I OVA complex showed a clear signal on LPMs isolated 24 h or 15 days after ID8^{ZGO} injection, suggesting that tumor antigens are continuously processed and presented on the cell surface (Figure 2C). To probe the ability to activate CD8⁺ T cells, we next isolated total LPMs, ZsGreen⁺ and ZsGreen⁻ LPMs, and SPMs from day 15 ID8^{ZGO}-challenged mice and cultured them with OVA-specific CD8⁺ T cells (OT-I). Total LPMs and ZsGreen⁺ LPMs induced robust T cell proliferation, while the ZsGreen⁻ fraction failed to induce T cell activation. SPMs triggered initial CD8⁺ T cell proliferation; however, cells arrested after a few cycles, resulting in a low proliferation index (Figures 2D and 2E). Consistently, total LPMs and ZsGreen⁺ LPMs triggered robust interferon γ (IFN γ) secretion by CD8⁺ T cells, while SPM and the ZsGreen⁻ LPM

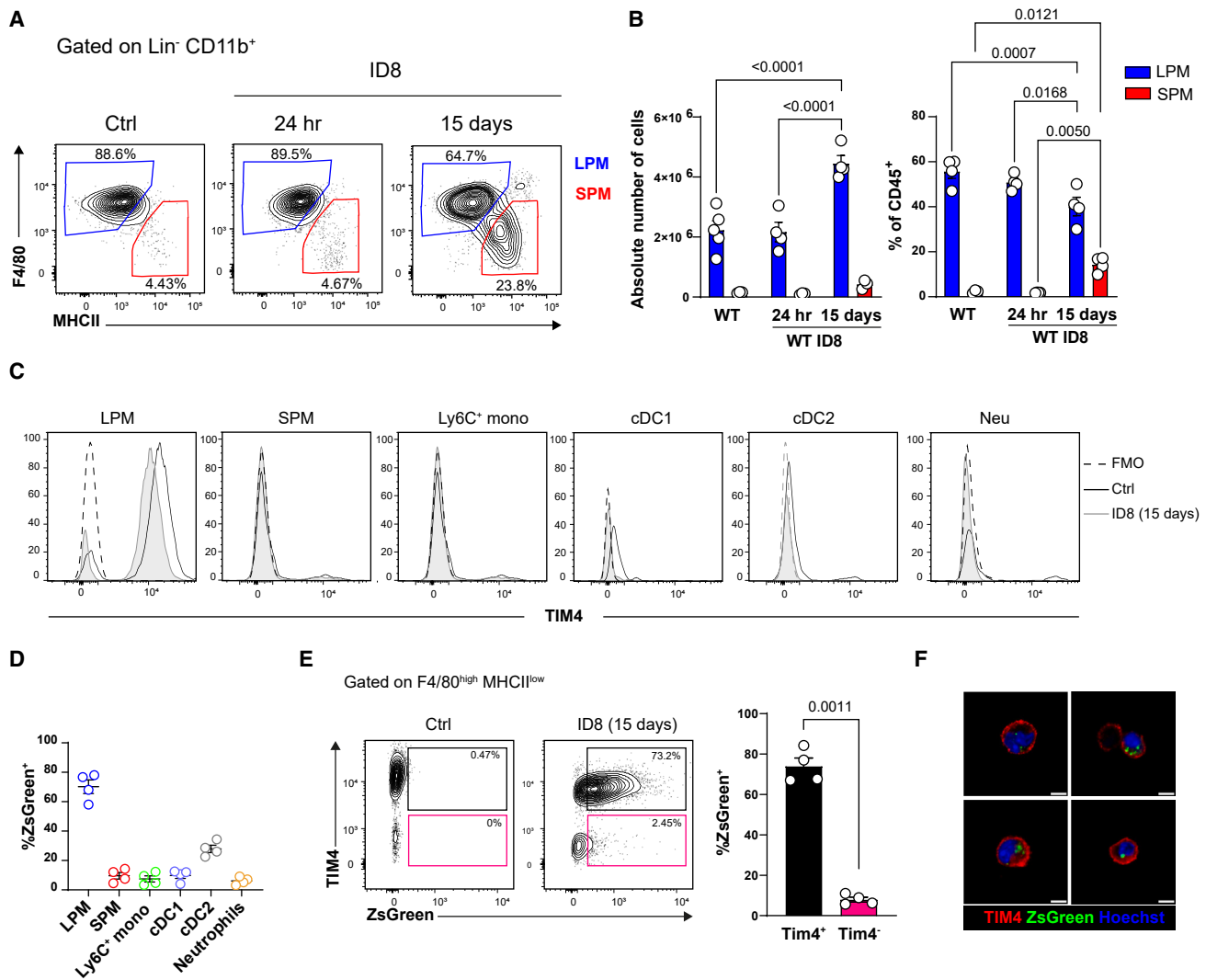


Figure 1. TIM4^{high} LPMs efficiently engulf ovarian cancer cells that colonize the peritoneal cavity

(A and B) Mice were challenged with ID8^{ZsGreen}, and peritoneal cells were collected after 24 h or 15 days. (A) Representative flow cytometry plots showing LPMs (F4/80^{high} MHC class II^{low}, blue) and SPMs (F4/80^{low} MHC class II^{high}, red) macrophages, gated on CD45⁺ CD11b^{high}, lineage⁻ cells (CD19, CD3, B220, NK1.1, Ly6C, and Ly6G). (B) Quantification of (left) absolute numbers and (right) fractions of LPMs and SPMs in resting (Ctrl) and tumor-bearing (ID8) animals. Data are from 3–4 animals. (C) Representative histograms showing TIM4 expression on LPMs, SPMs, Ly6C⁺ monocytes (Ly6C⁺ monos), type I dendritic cells (cDC1s), type II dendritic cells (cDC2s), and neutrophils (Neu) in Ctrl or ID8-challenged animals (15 days after challenge). Each peak is overlaid with the corresponding fluorescence minus one (FMO) controls (dotted line). (D) Quantification of tumor cell uptake plotted as percentage of ZsGreen⁺ cells within each population. *n* = 4, representing one of two independent experiments. (E) Representative dot plots and quantifications of uptake at day 15 by TIM4⁺ (black) and TIM4⁻ (pink) LPMs. *n* = 4. (F) Representative confocal images of sorted LPMs containing engulfed ZsGreen⁺ cancer cells. Scale bars, 5 μm. All data are represented as mean ± SEM. In (B), we used two-way ANOVA followed by Šidák's multiple-comparisons test. In (E), we used a paired *t* test.

fraction were poorly stimulatory (Figure 2F). Of note, at late tumor stages (60 days after challenge), LPMs were significantly less efficient at inducing CD8 T cell activation, indicating that tumor-derived factors modify the inherent properties of peritoneal resident macrophages and blunt the ability to cross-present (Figure S3B). To explore whether cross-presentation is a specific property of TIM4⁺ LPMs, we next tested lung-resident alveolar macrophages (AM), which lack TIM4 expression. LPMs and

AMs equally engulfed ID8^{ZsGreen} cells (Figure S3C); however, AMs were largely less efficient than LPMs at inducing the proliferation of OVA-specific CD8 T cells (Figure 2G). Together, these results indicate that, in the peritoneum, TIM4⁺ LPMs possess a superior capacity to acquire and cross-present engulfed tumor antigens. Moreover, AMs that lack TIM4 are unable to efficiently cross-present ingested tumor antigens, suggesting a specific role for the receptor in enabling cross-presentation.

TIM4 deficiency impairs the uptake and cross-presentation of tumor-associated antigens by LPMs

To directly examine the role of TIM4 during cancer cell uptake and cargo processing, we next injected ID8^{ZGO} into wild-type (WT) and TIM4-null recipients (Tim4 knockout [KO]).³³ The immune peritoneal compartment was analyzed 15 days after challenge. The influx of SPMs and the frequency of LPMs were equal between genotypes (Figure 3A and 3B). Proportions of cDCs, T cells, monocytes, and neutrophils were comparable, except for a slight decrease in neutrophils and an increment in the fraction of CD4 T cells in KO animals (Figure S4A). Cancer cell uptake by peritoneal phagocytes was similar between genotypes, except LPMs. Indeed, the fraction of ZsGreen⁺ LPMs was reduced from 67.8% ($\pm 9.5\%$) in the WT to 38.3% (± 7.1) in the Tim4 KO, indicating that optimal engulfment of cancer cells requires TIM4 and cannot be fully compensated by the remaining receptors (Figures 3C and S4B). TIM4-blocking antibodies resulted in a similar reduction of phagocytosis by LPMs, confirming a receptor-specific effect (Figure S4C). To understand how entry via TIM4 may affect subsequent cellular reprogramming, we next compared the transcriptional profiles of steady-state and ZsGreen⁺ WT and Tim4 KO LPMs. As a control, we verified that scavenger and phagocytic receptors were similarly expressed in the two genotypes, excluding compensatory effects (Figure S4D). Gene profiles at steady state were relatively comparable between genotypes, showing some changes in genes belonging to mitochondrial respiration (enriched in the WT) (Figures S4E and S4F). In contrast, the uptake of tumor cells induced a different response in the two genotypes (WT vs. WT-ID8 and TIM4 KO vs. TIM4KO-ID8; Figures S3G and S2A). Consistently, a direct comparison between WT and TIM4 KO LPMs containing phagocytosed cancer cells showed differential expression of genes and biological processes (Figures 3D and S4H). Specifically, uptake induced enrichment of genes regulating cellular metabolism (cellular respiration, glycolysis, and oxidative stress) in WT cells, while cholesterol biosynthesis and lipid metabolism were depleted with respect to TIM4-deficient cells. Notably, processes implicated in cytoskeletal dynamics, vesicular trafficking, inflammatory response, and antigen processing/presentation were also enriched in WT LPMs (Figure 3D). Genes defining these processes include kinesins, Rho GTPases, actin nucleation-promoting factors, IFN and cytokine signaling, proteasomal components, membrane transport, and MHC class I molecules. Of interest, genes governing cholesterol efflux and lipid metabolism were preferentially enriched in Tim4 KO cells (Figure 3E). Collectively, these data suggest that engulfment via TIM4 induces a proinflammatory transcriptional reprogramming of LPMs that includes upregulation of the machinery for antigen presentation. When TIM4 is absent, residual uptake via alternative routes triggers lipid reprogramming and cholesterol efflux, which is consistent with a decreased inflammatory profile.

TIM4 drives phagosomal actin coat formation during phagocytosis in LPMs

To further elucidate the mechanisms underlying TIM4-mediated cross-presentation, we next established *ex vivo* assays to examine post-engulfment trafficking of cargo in phagosomes containing the TIM4 receptor PS. At first, LPMs isolated from

resting WT or Tim4 KO mice were pulsed with CFSE-labeled apoptotic thymocytes for 15 min, washed, and chased for 15 or 30 min before fixation and labeling. We identified two categories of interactions: stage I, corresponding to cell-cell contact and phagocytic cup formation, and stage II, corresponding to internalization and phagosome closure. In WT LPMs at 15 min of chase, half of the interactions were in stage I and half in stage II, whereas stage II prevailed after 30 min (Figures 4A and 4C). A large fraction of TIM4-null LPMs were blocked in stage I at both time points, in line with impaired phagocytosis (Figures 4A and 4C). Nevertheless, approximately 27% and 32% had progressed to stage II after 15 and 30 min, respectively (Figures 4C, S5A, and S5B). Antibody labeling unveiled that TIM4 primarily localizes on the cell surface in resting macrophages (Figure S5C) but is rapidly translocated intracellularly upon exposure to apoptotic thymocytes (Figures 4A, S5D, and S5E). Notably, the membrane of nascent phagosomes was decorated by TIM4 (Figure 4A). In addition, we observed smaller intracellular TIM4⁺ structures, strongly overlapping with EEA1 and partially with LAMP1, whereas the association with the Golgi marker Rab6 was negligible (Figures S5D and S5F). TIM4 has been shown previously to engage with integrins to promote actin remodeling via Rho GTPases in artificial systems overexpressing the receptor and in zebrafish microglia.^{34,35} To investigate cytoskeletal dynamics downstream of receptor engagement in primary LPMs, we next tracked F-actin during uptake. In stage I conjugates, TIM4 enriched at the phagocytic cup, coinciding with F-actin. In closed phagosomes, F-actin overlapped with TIM4, forming a sharp ring at the phagosomal membrane. Of note, inhibition of integrin signaling by the phosphatidylinositol 3-kinase inhibitor LY294002 led to the formation of shallow abortive cups with a persistent thick actin base and inhibited the formation of organized phagosomes surrounded by actin cages (Figure S5G), as shown previously.³⁶ In TIM4-deficient LPMs, conjugates stalling in stage I similarly accumulated a thick F-actin interface at the site of interaction (Figures 4D and 4E), likely reflecting an impairment in downstream signaling to drive actin disassembly. Moreover, nascent phagosomes in TIM4-null cells were almost completely devoid of surrounding actin (Figures 4A and 4F), further supporting that TIM4 orchestrates phagosomal architecture. To emphasize more specifically the role of TIM4-PS interactions, we next employed deformable acrylamide co-acrylic acid microparticles (DAAMps) featuring the size and mechanical rigidity of apoptotic cells (diameter, $\sim 6.2 \mu\text{m}$; Young's modulus E_y , 5 kPa) that were functionalized with PS (PS-DAAMps).^{37,38} As an additional advantage, PS-DAAMps as artificial targets permit unequivocal assessment of LPM-derived cellular structures, excluding confounding cellular factors from thymocytes. Phagocytosis of PS-DAAMps was reduced in TIM4 KO cells, similar to apoptotic cells (Figures S5A and S5B). Consistent with data obtained with thymocytes, PS-DAAMps induced TIM4 and actin recruitment at the phagocytic cup and phagosomes were decorated by a thick actin coat colocalized with TIM4. Moreover, uptake of PS-DAAMps by TIM4-null LPMs showed actin thickening at sites of failed phagocytosis and reduced actin involvement in nascent phagosomes (Figures 4B, 4G, and 4H). Taken together, these results indicate that engagement of TIM4 with PS triggers actin

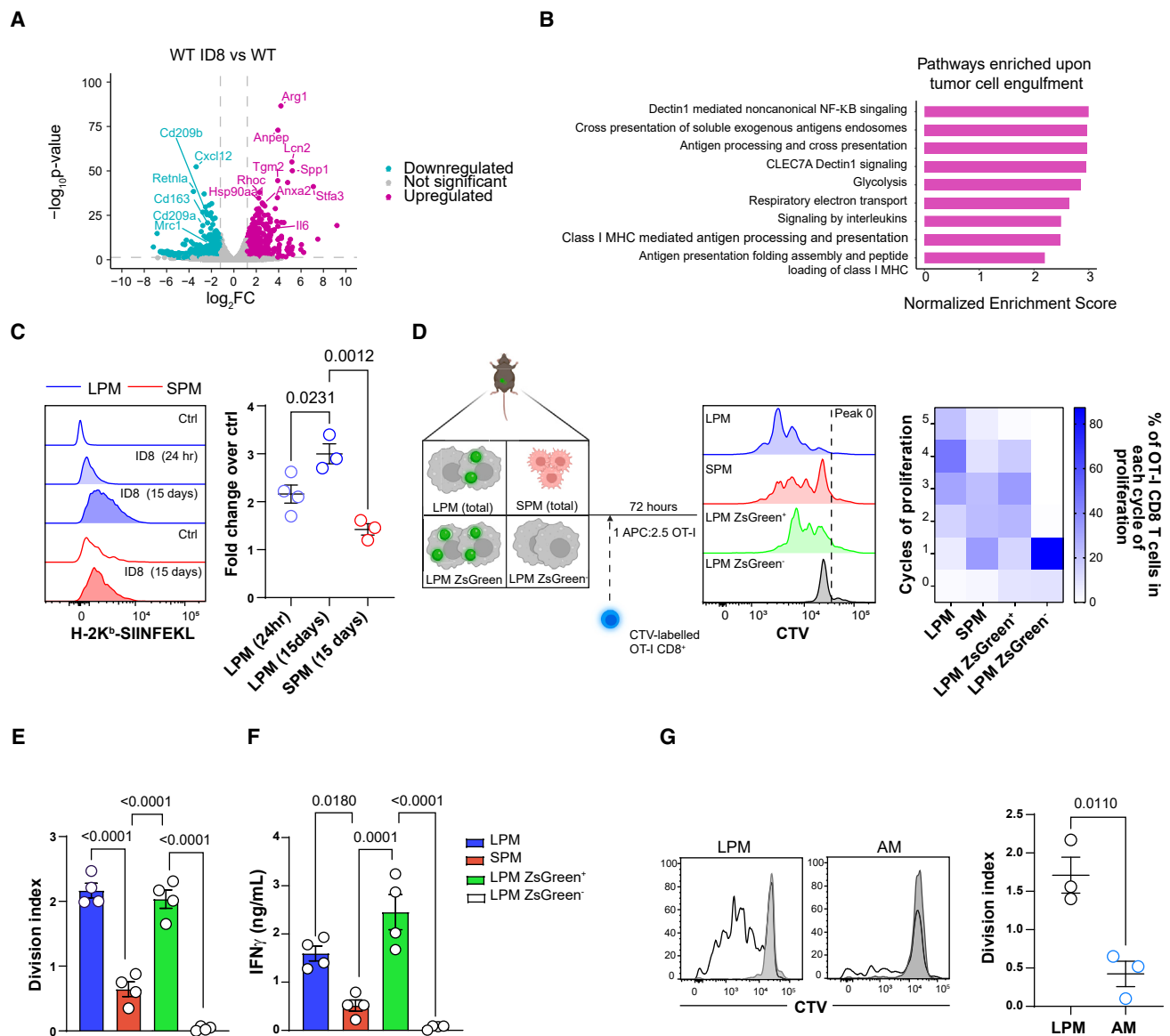


Figure 2. Uptake of cancer cells by LPMs induces transcriptional remodeling and cross-presentation of tumor-derived antigens

(A) Bulk RNA-seq of cell-sorted, tumor-loaded LPMs (ID8) or control LPMs (Ctrl) was performed 24 h after challenge. The volcano plot shows genes upregulated (magenta) and downregulated (cyan) in LPM-ID8 vs. control (\log_2 fold change > 1.5 and < -1.5 , respectively; $p < 0.05$, $n = 3$ per group).

(B) Gene set enrichment analysis (GSEA) was performed against Reactome gene sets of control LPMs and LPM-ID8. NES, normalized enrichment score.

(C) Histograms show labeling by 25D1.16 (specific for the MHC class I-OVA complex) on LPMs and SPMs isolated 24 h and 15 days after challenge with ID8-OVA and the corresponding quantification (fold change over control). $n = 3\text{--}4$ animals/experiment. Data represent of one of two independent experiments.

(D) LPMs, SPMs, and LPMs, ZsGreen⁺ and ZsGreen⁻, were sorted 15 days after ID8^{ZGO} injection and co-cultured with cell-trace violet (CTV)-labeled naive OVA-specific CD8 T cells (OT-I), as depicted. Also shown are primary histograms and heatmap quantification of the fraction of proliferated OT-I cells in each cycle of division.

(E) OT-I cell proliferation plotted as division index.

(F) IFN γ secretion by OT-I cells after 72 h of co-culture.

(E and F) $n = 4$; each point is pooled from 2 animals.

(G) LPMs and lung alveolar macrophages (AMs) were loaded with apoptotic ID8^{ZGO} and co-cultured with CTV-labeled OT-I cells. Histograms show proliferation profiles induced by non-pulsed LPMs or AMs (filled) or ID8^{ZGO} pulsed cells (empty) and the corresponding division index. $n = 3$. All data are represented as mean \pm SEM. In (C), we used one-way ANOVA followed by Dunnett's multiple-comparisons test. In (E) and (F), we used one-way ANOVA followed by Sidak's multiple-comparisons test. In (G), we used an unpaired t test.

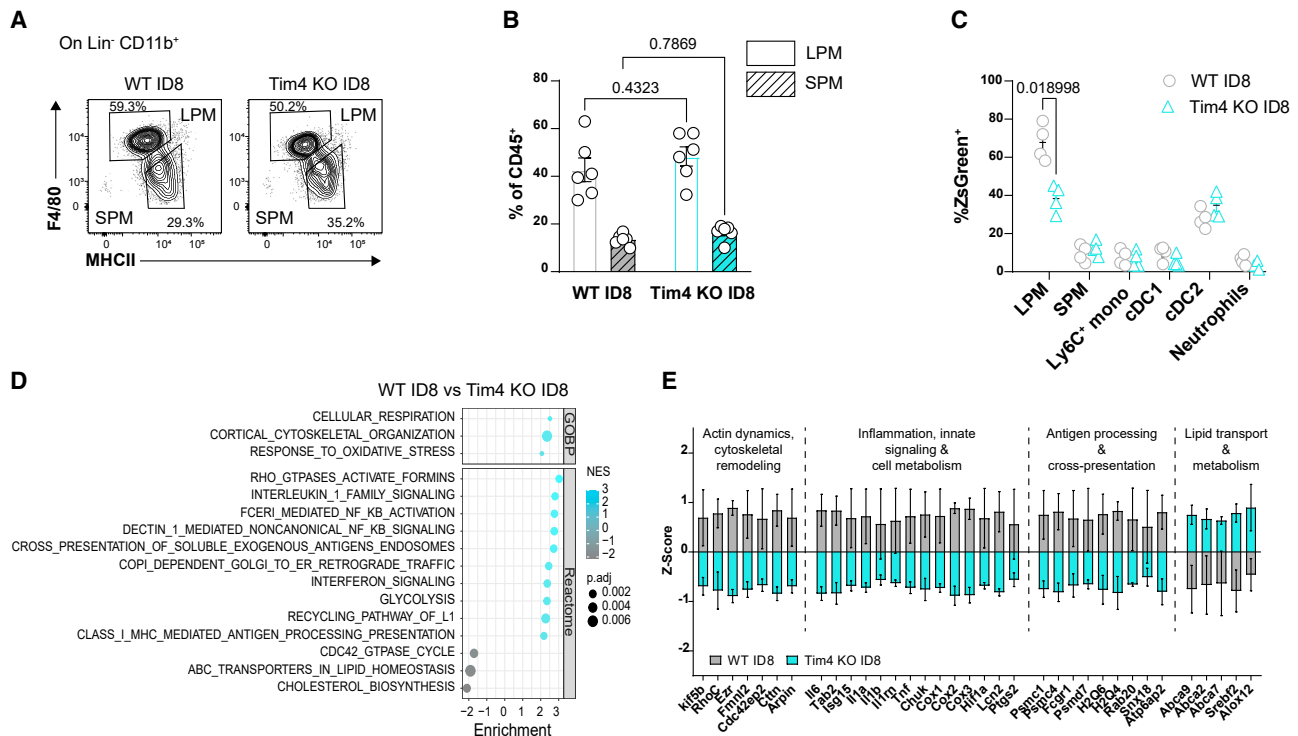


Figure 3. Tim4 controls transcriptional remodeling of LPMs

(A and B) WT and Tim4 KO mice were injected intraperitoneally with ID8^{ZGO}, and peritoneal cells were isolated after 15 days. Shown are (A) representative flow cytometry dot plots and (B) quantification of SPMs and LPMs in the peritoneal cavities of the WT and Tim4 KO. *n* = 4–5 animals/experiment, representing one of three independent experiments.

(C) The phagocytic index is plotted as the fraction of ZsGreen⁺ cells among total cells in each of the indicated populations. *n* = 4, data are representative of one of two independent experiments.

(D) GSEA was performed against GO and Reactome gene sets of WT and Tim4 KO LPM-ID8. The dot plot shows selected pathways significantly enriched in WT LPM-ID8.

(E) Distribution of Z scores of genes defining the enriched pathways in WT-ID8 related to four indicated process modules. All data are represented as mean ± SEM. In (B), we used two-way ANOVA followed by Šídák’s multiple-comparisons test. In (C), we used a multiple t test followed by Welch correction.

remodeling in LPMs, driving the biogenesis of actin-sealed phagosomes.

TIM4-driven actin coats delay docking of lysosomal markers on phagosomes

We next examined the kinetics of phagosome maturation in WT and TIM4-deficient LPM post internalization of apoptotic cargo. To track specific events during cargo processing, we co-labeled LPMs with a live cell actin probe (siR-Actin) and a marker of phagolysosomal fusion (LAMP1). In addition, we exploited commercially available antibodies against ATP6V1A (a subunit of the vacuolar proton pump V-ATPase, which initiates acidification of the phagosomal lumen). In agreement with the data in Figure 4, early phagosomes (15 min post uptake) were enclosed by a dense siR-Actin signal, layering the phagosomal membrane. Small V-ATPase vesicles and larger lysosomal organelles were found approaching the phagosomes but were not crossing the actin barrier (Figures 5A–5C). After 30 min, the actin coat disassembled leaving actin-free docking sites where V-ATPase and LAMP1 began to accumulate. At later time points (45 min), the internalized cargo was surrounded by LAMP1 vesicles and

showed signs of fragmentation (Figures 5A–5C). In sharp contrast, cargo taken up by TIM4 null LPM was rarely enclosed in organized actin-coated phagosomes but was rather nibbled with degradation occurring before cargo internalization was completed (Figure 5A). Strikingly, cargo overlapped with dense V-ATPase and LAMP1 positive vesicles already at early time points (15 and 30 min). After 45 min, cargo internalized by TIM4 deficient LPM was mostly degraded and entirely contained within the lumens of lysosomal vesicles with proximal V-ATPase (Figures 5A–5C). Additionally, scoring the size of cargo as intact, partially or fully fragmented, revealed a significantly faster accumulation of degraded material within Tim4 KO cells (Figure 5D). Rapid LAMP1 acquisition was similarly observed when feeding WT or Tim4 KO LPMs with apoptotic ID8, suggesting that TIM4 controls downstream trafficking independently of the cargo nature (Figures S6A and S6B).

TIM4-deficient LPMs show accelerated acidification and cargo degradation

Next, we set up two complementary flow cytometry-based assays to quantitatively assess acidification and cargo degradation. In the

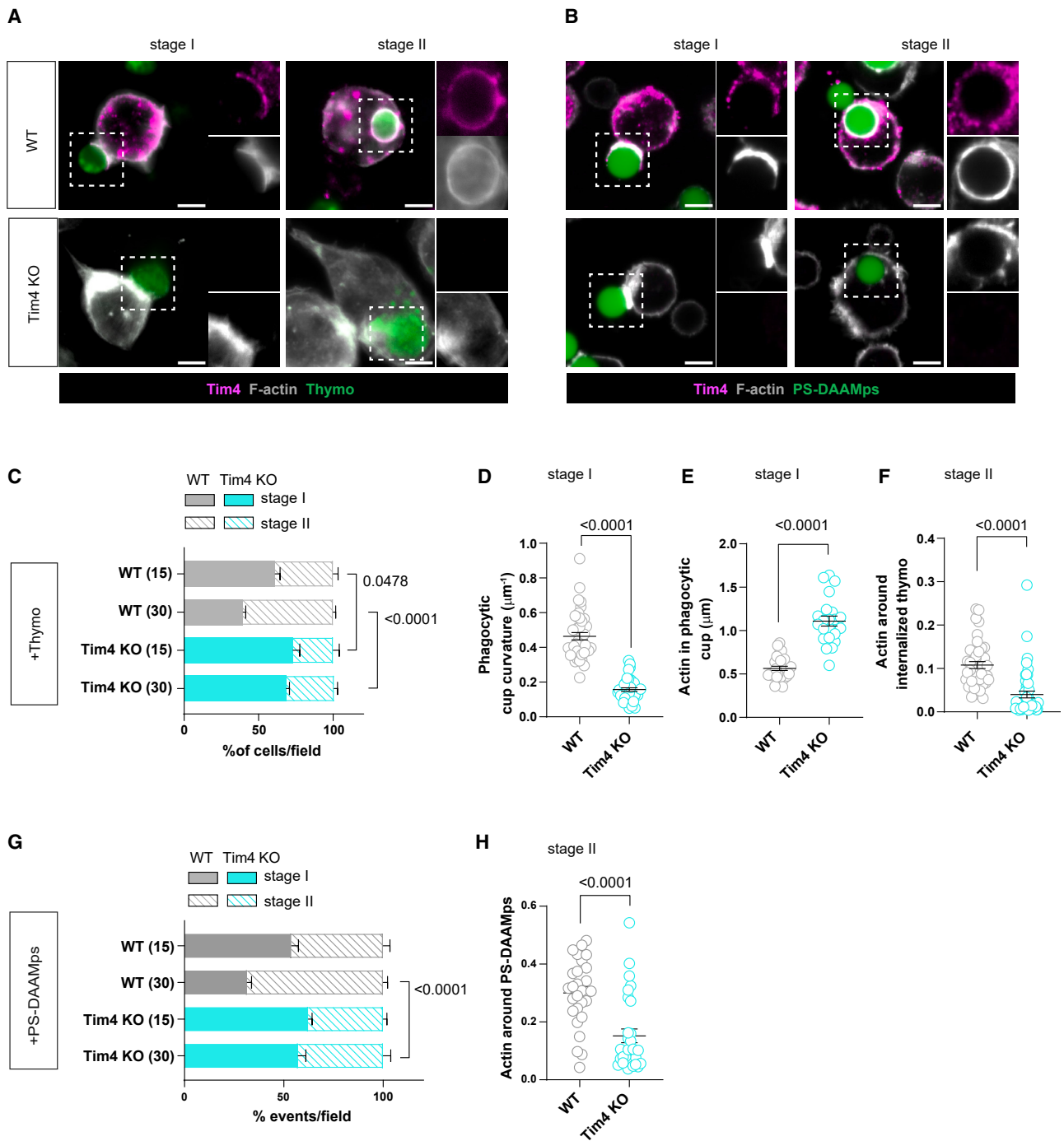


Figure 4. Tim4 localizes with actin at the phagocytic cup, and it is internalized in nascent phagosomes

(A and B) WT and Tim4 KO LPMs isolated from naive mice were pulsed for 15 min with CFSE-labeled apoptotic thymocytes (A) or fluorescein isothiocyanate (FITC) PS-DAAMps (B) and chased for 15 or 30 min. After fixing, cells were stained using antibodies to TIM4 and phalloidin to label F-actin. Representative confocal images show the two stages of phagocytosis used for classifying the interactions. Scale bars, 5 μm .

(C–F) Pulse with thymocytes.

(C) Quantification of the number of events in stage I and stage II in WT and Tim4 KO LPMs after 15 or 30 min of chase. Data are representative of $n > 30$ events/fields containing > 15 LPMs each, pooled from 3 independent experiments.

(D) Curvature index of the phagocytic cup calculated on cells in stage I.

(E) Thickness of F-actin in the phagocytic cup. $n > 15$ cells from 2 independent experiments.

(legend continued on next page)

first, dying thymocytes were loaded with CypHer5E, a pH-sensitive probe that emits fluorescence upon acidification in acidic organelles (Figure S6C) and CTV, which is stable across a wide range of pH, as a control for uptake. WT or Tim4 KO LPMs were fed with apoptotic thymocytes *ex vivo*, and cells were analyzed by flow cytometry to follow the kinetics of acidification. Fluorescence intensity increased over time in both genotypes. However, the increment started earlier in Tim4 KO cells, and it was consistently higher than in WT cells, at every time point analyzed (Figures 5E and 5F). Notably, inhibiting acidification by bafilomycin A1 (an inhibitor of V-ATPase) reduced the index of acidification of Tim4 KO cells to the level of WT cells. To explore the role of the NADPH complex and reactive oxygen species (ROS) in phagosomal acidification, we used the NADPH oxidase 2 inhibitor (NOX inhibitor) diphenyleneiodonium (DPI) in the cypHer-based acidification assay. The treatment did not affect the acidification rate of Tim4 KO cells; however, it significantly accelerated acidification in WT cells (Figure S6D). This result suggests that TIM4-induced phagosomes trigger ROS production, which could impact on acidification of the lumen^{39,40} and oxidative damage of the limiting membrane.⁴¹

We next developed an assay to measure cargo degradation. PS-DAAMps were functionalized with a mixture of BSA coupled to Alexa 647 (a pH-insensitive dye) and DQ-BSA, a self-quenched conjugate that emits bright fluorescence only upon cleavage in proteolytic organelles. After a 15-min pulse, we tracked the increment in fluorescence intensity over time and expressed it as index of degradation. As shown in Figure 5G, degradation was faster and larger in Tim4 KO cells than in the WT at every time point tested, corroborating our findings by confocal imaging. To understand whether slower maturation kinetics in LPMs are specific for targets engulfed via TIM4 or applies to other entry routes, we next functionalized DAAMps with immunoglobulin G (IgG) to engage FcReceptor-mediated phagocytosis. WT and TIM4-null LPMs were exposed to the particles for 15 or 30 min, and the phagosomal structures were analyzed by confocal imaging. No major differences were detected in terms of phagocytic index, actin coat formation, acquisition of phagosomal LAMP1 signal, and degradation between the two genotypes, suggesting that uptake and processing of IgG cargo is intact in TIM4-null cells (Figures 5H and S7A–S7D). Collectively, these results prove that TIM4-mediated engulfment induces stepwise progression of the ingested cargo, preserving antigens for cross-presentation.

Tim4 is required for cross-presentation of cancer-associated antigens by LPMs

To understand whether cross-presentation by LPM drives antitumoral T cell responses *in vivo* and to evaluate the functional

impact of accelerated antigen degradation in Tim4 KO LPMs, we next challenged WT and Tim4 KO animals with ID8^{ZGO}. Labeling LPMs with pMHC class I OVA-specific antibodies 15 days after tumor challenge showed a consistently reduced signal in TIM4 KO cells (Figure 6A). In line with this result, WT cell-sorted LPMs (total or tumor cell-enriched, ZsGreen⁺) plated with OT-I induced significantly larger T cell proliferation and IFN γ release than Tim4 KO cells, confirming blunted cross-presentation (Figures 6B and 6C). Furthermore, the frequencies of endogenous tumor antigen-specific CD8 T cells measured by pentamer staining and T cell effector functions were higher in WT hosts (Figures 6D and 6E). Reduced cross-presentation and CD8 T cell activation in Tim4 KO hosts were confirmed immediately after cancer cell encounter (24 h), confirming that LPMs are intrinsically impaired (Figures S8A–S8C). To validate the PS-TIM4 engulfment axis as a driver of cross-presentation, we prepared liposomes including PS (PS-lipo) or phosphatidylcholine (PC-lipo) as a control (Figure S8E). Liposomes were functionalized to encapsulate DQ-BSA/Alexa 647-BSA to track degradation or the antigen OVA. In line with the other data, PS-lipo was specifically targeted to LPMs, and degradation was accelerated in TIM4 KO LPMs (Figures S8F and S8G). *In vivo* delivery of OVA antigen via PS-lipo (PS-lipo-OVA) induced robust proliferation of adoptively transferred OT-I cells, while PC-OVA liposomes or PS-liposomes containing a control protein induced little or no T cell proliferation (Figure S8H), confirming the ability of TIM4⁺ LPMs to take up and cross-present tumor antigens and the potential of TIM4 targeting. Finally, we evaluated the impact of LPM-driven cross-presentation on tumor progression. Toward this goal, we adoptively transferred OT-I to increase the frequency of tumor-specific T cells. Animals were challenged with ID8 cells, and tissues were harvested after 15 days to focus on early stages of tumor progression. Immune profiling of the T cell compartment confirmed enhanced expansion of transferred OT-I cells and upregulation of surface effector T cell markers and cytotoxicity (Figures 6F–6I) in WT hosts. Importantly, the number of cancer cells in the peritoneum of TIM4 null animals was significantly higher in Tim4 KO. Immunohistochemical analysis of the omentum, a known site of premetastatic colonization by ovarian cancer cells,⁴² confirmed significantly larger tumor nodules in TIM4-null animals than in the WT (Figures 6J and 6K). In summary, we conclude that TIM4 expression on LPMs enables the detection of antigens within dead cancer cells to promote cross-presentation and immune surveillance of the peritoneal cavity in the early stages.

DISCUSSION

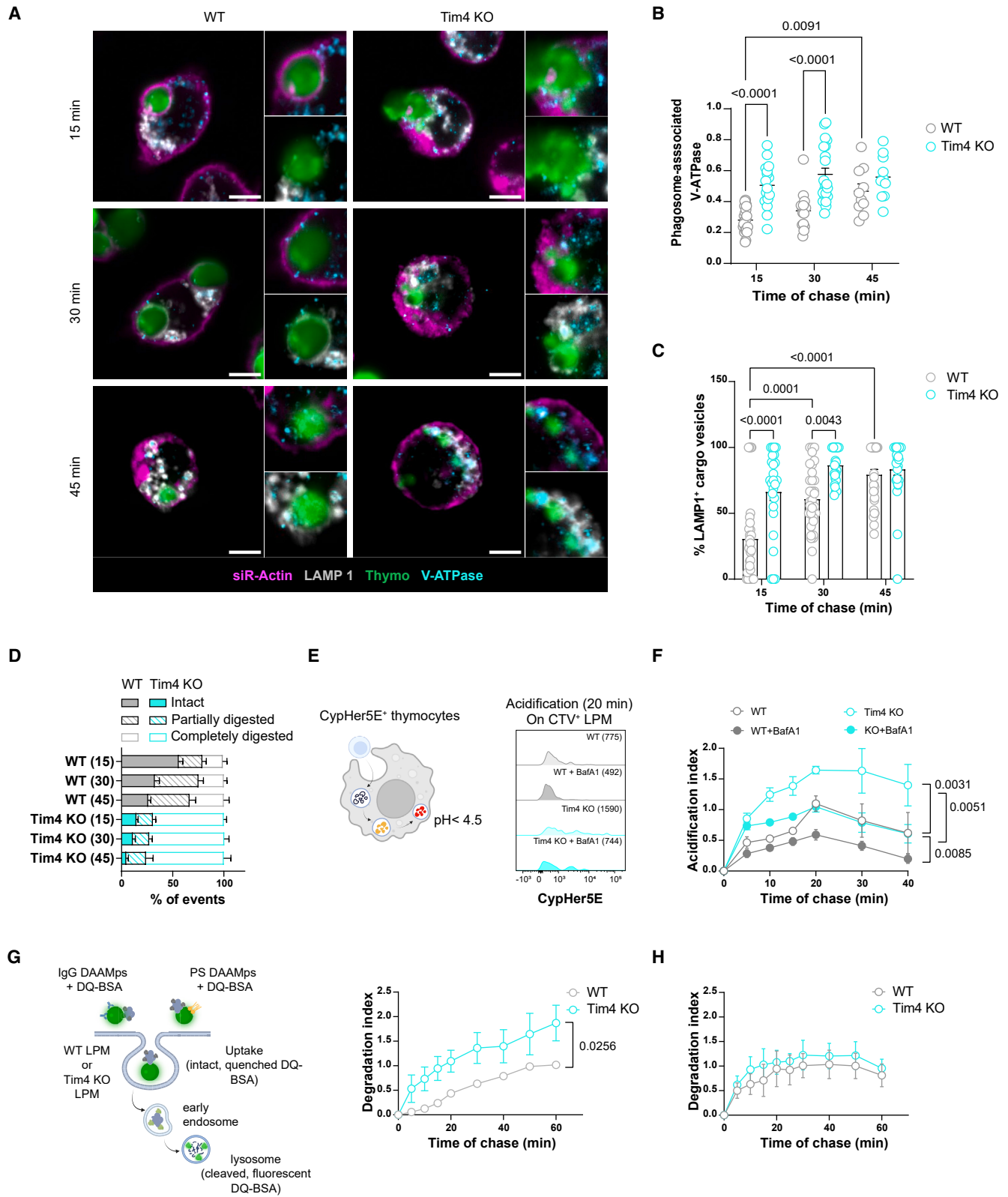
Understanding the specific function of diverse subsets of TAMs at different stages along tumor progression is key for developing

(F) F-actin integrated density in nascent phagosome around the cargo, normalized to total F-actin density within each cell. $n > 20$ cells from two independent experiments.

(G and H) Pulse with PS-DAAMps.

(G) Quantification of the number of events in stage I and stage II in WT and Tim4 KO LPMs at the indicated time points. Data are representative of $n > 15$ events/fields containing at least 15 LPMs each, pooled from 3 independent experiments.

(H) F-actin integrated density in nascent phagosome around the internalized PS-DAAMps normalized, with F-actin density within each cell. $n > 15$ cells from 2 independent experiments. All data are represented as mean \pm SEM. In (C) and (G), we used two-way ANOVA followed by Sidák's multiple-comparisons test. In (D)–(F) and (H), we used an unpaired t test.



(legend on next page)

a novel macrophage-centered therapeutic axis. Here we demonstrate that, shortly after seeding in the peritoneum, LPMs can transiently cross-present tumor antigens. This exquisite function of LPMs is supported by the PS receptor TIM4, which maximizes internalization of cancer cells, regulates transcriptional circuits induced by engulfment, and orchestrates phagosomal maturation to promote cross-presentation of tumor antigens.

The role of LPMs in cancer has been addressed mostly in the context of antigen presentation-independent functions and at late stages of tumor progression. Consistent reports have shown that tissue-resident LPMs of embryonic origin proliferate *in situ* and progressively incorporate inflammatory monocytes under tumor-derived cues.^{27,32,43,44} In parallel, LPM shift from a tumoricidal, high-inflammatory profile at early stages to an anti-inflammatory profile in advanced tumors. The latter is characterized by high oxidative phosphorylation and glycolysis, enhanced mitophagy, altered lipid metabolism, increased cholesterol efflux, and dominance of interleukin-4 signaling over IFN γ signaling.^{20,43,45} Our data, focusing on very early events of metastatic colonization of the peritoneum, unveil a distinct side of LPMs. Indeed, cancer cell recognition by naive LPMs triggers vigorous uptake, followed by an inflammatory and metabolic response that culminates in the presentation of ingested antigens on MHC class I. The induction of an inflammatory gene program also indicates that the uptake of cancer cells, unlike normal apoptotic cells,⁴⁶ is not silent and may contribute to remodeling of the compartment, as described recently in monocyte-derived macrophages expressing TREM2.⁴⁷ Interestingly, the capacity of LPMs to cross-present was strongly inhibited in late tumors, which is consistent with an active educational mechanism that shapes resident macrophages toward a pro-tumoral phenotype.

Cross-presentation of cancer antigens has been described previously for CD206⁺ monocyte-derived cells¹³ upon CD47 blockade in bone marrow-derived macrophages,⁴⁸ red pulp splenic macrophages,⁴⁹ and lymph node-resident CD169⁺ cells.^{14,50} So far, intrinsic cross-presentation by a clearly defined population of *bona fide* resident macrophages such as LPMs is unprecedented and suggests a new layer of cancer immune surveillance at sites of metastatic colonization.

Several cellular adaptations have been characterized, especially in dendritic cells, that enable cross-presentation by phago-

cytes. First, receptors that mediate the uptake of dead cells, such as CLEC9A-DNGR-1, CD36, AXL, SCARF-1, and TIM3 have been implicated in cross-presentation of ingested antigens by dendritic cells.^{41,51–55} Second, depending on the cellular context, cross-presentation has been shown to be enabled by slow processing of ingested cargo, which preserves antigen integrity followed by active transfer of phagosomal antigens to the cytosol to intersect the conventional MHC class I pathway or by specialized pathways of vacuolar trafficking.^{40,41,56–58} Our data suggest that TIM4 may enable cross-presentation in subsets of macrophages, similar to what we have found in lung cDC1s.²⁹ In this respect, the finding that AMs (which do not express the receptor) are unable to cross-present is notable and solicits further investigations to understand the biological significance of phagocytic receptors controlling cross-presentation on diverse subsets of TRMs.

The mechanism of cross-presentation that we propose is in line with past reports showing that phagosomal actin nucleation delays maturation by physically preventing phagolysosomal fusion to protect the cargo from fast degradation.^{59,60} Second, a recurrent and persistent actin layer is also speculated to assist in “chewing before digestion,” allowing larger particles with their native structures to be available to macrophages for cross-presentation.⁶¹ Conceivably, actin remodeling in LPMs entails TIM4 bridging with fibronectin to engage β 1 integrin, PI3K, and Rho GTPase activation, as shown previously in artificial systems expressing the receptor.^{34,62–64} Remarkably, a recent study has shown that grafting TIM4 on engineered T cells confers them with the ability to cross-present.⁶⁵ Based on our data and the current models, we propose that delayed acidification in TIM4 phagosomes prevents antigens from fast destruction, which, in combination with ROS-mediated damage of the phagosomal membrane, may facilitate the translocation of intact polypeptides to the cytosol to enter the endogenous pathway of MHC class I presentation.^{41,66,68}

Conflicting with our findings, previous reports have suggested that TIM4 expression by TAMs and bone marrow-derived macrophages controls LC3-mediated phagocytosis, a form of non-canonical autophagy that accelerates antigen degradation, blunting cross-presentation.^{28,67} This discrepancy may depend on the different cell types analyzed (mono and bone

Figure 5. Tim4 controls phagosome maturation and cargo degradation

(A) Representative confocal images showing actin (siR-Actin), V1A subunit of V-ATPase, and lysosome (LAMP1) labeling in WT and Tim4 KO LPMs pulsed with CFSE-labeled thymocytes and chased for 15, 30, or 45 min. Scale bars, 5 μ m.

(B) Quantification of normalized V1A intensity around engulfed thymocytes. $n > 20$ cells from 2 independent experiments.

(C) Bars show the fraction of internalized cargo associated with LAMP1 vesicles. $n > 20$ cells; one of three independent experiments is represented.

(D) The fraction of intact, partially digested, or completely digested intracellular cargo was quantified for each of the indicated time points. Data represent $n > 10$ fields with >15 cells per time point, per group.

(E and F) CypHer5E-based acidification assay. WT or Tim4 KO LPMs were pulsed for 15 min with apoptotic thymocytes loaded with CypHer5E and CTV to normalize uptake. The fluorescence intensity of CypHer5E on CTV⁺ LPMs was acquired for up to 40 min, and the acidification index was calculated. Filled circles show the acidification index in cells treated with bafilomycinA1. $n = 3$ independent experiments.

(G and H) Left: Schematic of the DQ-BSA-based assay using IgG- or PS-DAAMps. LPMs were pulsed for 15 min with PS-DAAMps (G) or IgG-DAAMps (H) functionalized with DQ-BSA and A647 BSA (LPM-DAAMps ratio, 1:10). The median fluorescence intensity of DQ-BSA was recorded over time up to 60 min, and the degradation index was calculated. $n = 3$ independent experiments. All data are represented as mean \pm SEM. In (B), we used two-way ANOVA followed by Tukey’s multiple-comparisons test. In (C), we used two-way ANOVA followed by Sidák’s multiple-comparisons test. In (F), statistical analysis was conducted by non-linear regression, fitting the data in “one phase association” model to compute the plateau for individual experiments. The resulting plateau values were analyzed by two-way ANOVA followed by Tukey’s multiple-comparisons test. In (G) and (H), statistical analysis was conducted by non-linear regression as in (F). The resulting plateau values were analyzed by paired t test.

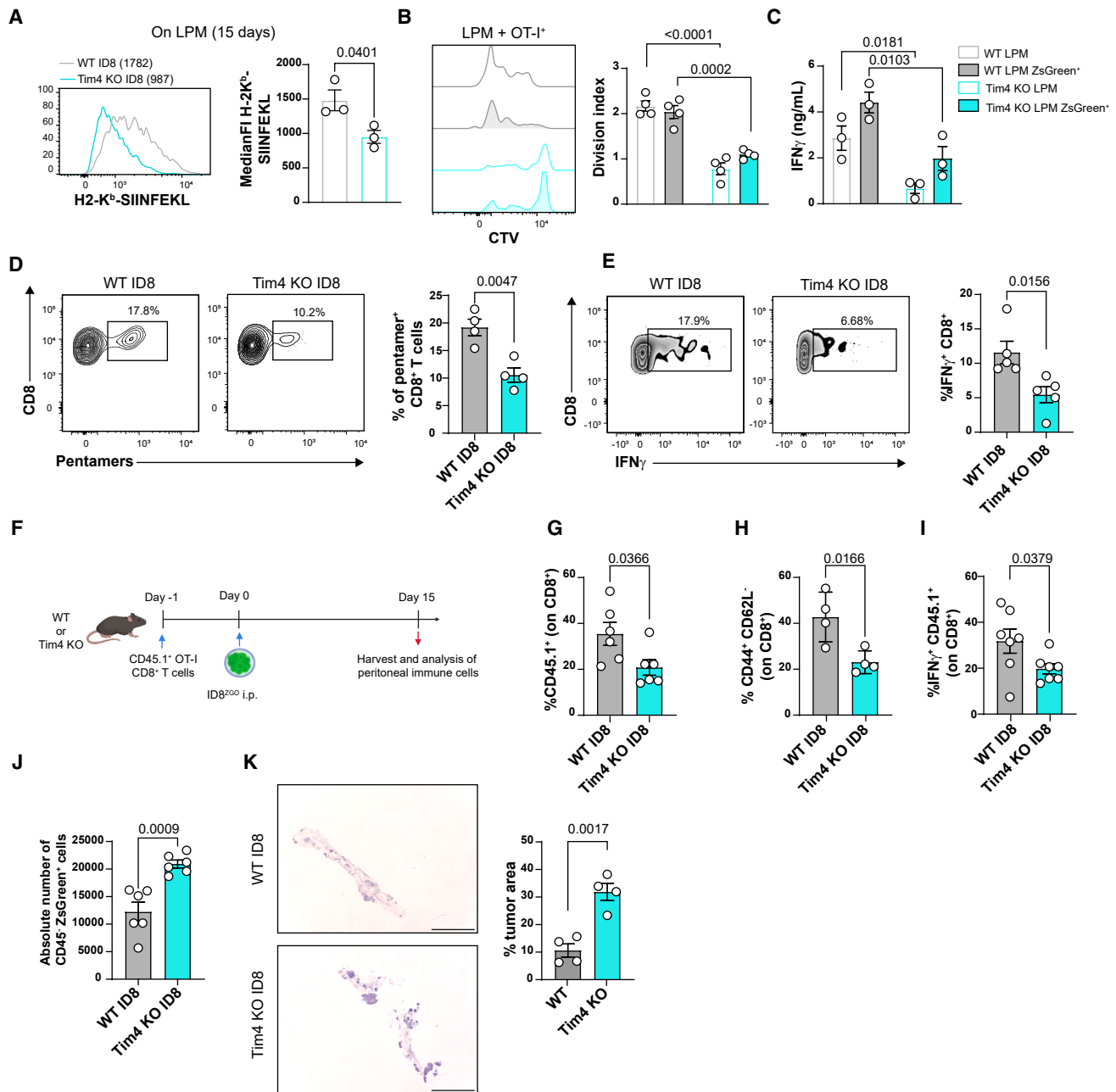


Figure 6. Anti-tumoral CD8 T cell responses to peritoneal metastasis depend on cross-presentation by TIM4⁺ LPMs

(A) Histograms show MFI of WT and TIM4 KO LPMs stained with the 25D1.16 antibody, 15 days after ID8^{ZGO} tumor induction. *n* = 3; one of two independent experiments is represented.

(B) Representative histograms and division index of OT-I proliferation induced *ex vivo* by total or ZsGreen⁺ LPMs sorted from the WT and Tim4 KO, 15 days after challenge. *n* = 4.

(C) IFN γ production in the supernatant of LPM-OT-I CD8 T cell co-cultures as measured by ELISA. *n* = 4.

(D and E) *In vivo* activation of peritoneal tumor-specific CD8 T cells (identified by OVA-specific Pro-5 pentamers) in WT and Tim4 KO animals, 15 days after challenge. Shown are representative dot plots and quantification. *n* = 4, representing one of 3 independent experiments.

(E) Intracellular production of IFN γ by endogenous CD8 T cells restimulated *ex vivo* with OVA class I peptide. Shown are representative dot plots and quantification. *n* = 5.

(F) Schematic of the experimental setup for (G)–(I).

(G–I) The expansion (G), effector phenotype (CD3⁺ CD8⁺ CD44⁺ CD62L⁻) (H), and IFN γ production (I) by adoptively transferred CD45.1 OT-I CD8 T cells 15 days after tumor challenge. *n* = 4–7, pooled from 2 independent experiments.

(legend continued on next page)

marrow-derived macrophages vs. resident LPMs), suggesting a context-dependent function of the receptor. It is also important to note that we and others^{24,69} could not detect TIM4 expression in bone marrow-derived macrophages.

Interestingly, our transcriptomic analysis revealed a relatively higher expression of several genes involved in lipid transport in TIM4-null macrophages (Figures 3E and S4H). This includes members of the ABC family, such as *Abca2* and *Abca7*, known as lipid transporters;⁷⁰ *Abca9*, a speculated mediator of lipid homeostasis;⁷¹ as well as *ApoE*, which reportedly drives lipid transport and immunosuppression via induction of *Cxcl1* and *Cxcl5*.⁷² This transcriptional profile suggests increased lipid export in TIM4-null cells, which would be consistent with the inflammatory genes profile.^{32,73} A further intriguing link between TIM4 and lipid metabolism recently emerged in adipose tissue macrophages, where the receptor was shown to mediate the transfer of scavenged lipids into lysosomes, promoting lysosomal functions and ABCA1-mediated post-prandial cholesterol transport.²⁶ Thus, establishing the precise causal link between TIM4 regulation of lipid metabolism and cross-presentation remains an interesting area for future investigations.

The ability of TRMs to cross-prime CD8⁺ T cells and drive differentiation into polyfunctional effectors has been documented before in the context of breast cancer. Importantly, macrophages mediating this function display high TIM4 expression and are associated with better prognosis in patients.⁸ In the present study, we also observed immediate activation of tumor-specific CD8⁺ T cells by TIM4⁺ macrophages and accumulation of cytotoxic CD8⁺ T cells on day 15, which were significantly impaired in TIM4-null animals, leading to accelerated tumor growth. Our observation remains confined to the early stages of tumorigenesis. At late stages, the peritoneal cavity is heavily infiltrated by mono-derived macrophages, which instead mediate exhaustion and deactivation of T cells.²⁷ Therefore, cell-intrinsic changes in LPMs, combined with massive infiltration by immune suppressive mono-derived cells, collectively override immune surveillance. Currently, the lack of tools to conditionally ablate TIM4 on LPMs at defined time points precludes the evaluation of later outcomes.

In summary, our findings reveal an important intracellular function of TIM4 that, besides mediating uptake of PS-expressing cells, contributes to channel ingested antigens for cross-presentation, enabling cancer immune surveillance at initial stages.

Limitations of the study

The unavailability of tools to conditionally delete TIM4 on LPMs at defined time points precluded the evaluation of anti-tumoral responses at late stages. The bulk RNA-seq used in this study does not capture the diversity in subpopulations of LPMs, and the observed changes in inflammatory circuits and lipid metabolism profiles remain to be validated at the protein level. The

mechanisms accounting for TIM4-mediated cross-presentation have not been entirely dissected at the cellular level due to limitations in quantity, quality, and difficulties in the manipulation of primary LPMs. This also restricted our immunofluorescence analysis of acidification to the use of commercially available α ATP6V1A, which has shown variable staining signals in different cell types.⁷⁶ LPMs deprogram when isolated from the peritoneal cavity, showing a rapid decline in TIM4 expression. This has limited our analysis to confocal imaging and fast flow cytometry-based assays, precluding KO/overexpression studies or biochemical analysis.

STAR★METHODS

Detailed methods are provided in the online version of this paper and include the following:

- KEY RESOURCES TABLE
- RESOURCE AVAILABILITY
 - Lead contact
 - Materials availability
 - Data and code availability
- EXPERIMENTAL MODEL AND STUDY PARTICIPANT DETAILS
 - Mouse models
 - Cell lines and cell culture
- METHOD DETAILS
 - Establishment of peritoneal tumors
 - H&E of omenta
 - Isolation of murine peritoneal and omental cells
 - Flow cytometry
 - Induction of apoptosis
 - Ex vivo priming of OT-I cell by cell sorted macrophages
 - Ex vivo phagocytosis and cross-presentation by peritoneal and alveolar macrophages
 - Bulk RNA sequencing of ZsGreen+ LPM and analyses
 - Preparation of IgG and PS-functionalized DAAMps
 - Preparation and characterization of PS and PC liposomes
 - Degradation assay (DQ-BSA)
 - Tracking the rate of lysosomal acidification using cypHer labeled thymocytes
 - Confocal imaging of peritoneal macrophages and quantification
 - Detection of OVA-MHC-I complexes on surface of peritoneal macrophages
 - Adoptive transfer of OT-I CD8 T cells and *in vivo* proliferation
 - Activation of endogenous anti-tumor CD8⁺ T responses
- QUANTIFICATION AND STATISTICAL ANALYSIS

(J) Absolute number of CD45⁺ ZsGreen⁺ tumor cells in the peritoneal cavity of WT and Tim4 KO mice 15 days after challenge with ID8^{ZGO}. *n* = 6, pooled from two of four independent experiments.

(K) Representative H&E sections and quantifications of tumor nodules on mouse omenta collected from WT and Tim4 KO mice 15 days after ID8^{ZGO} challenge. The percentage of tumor area is plotted as a function of total area of the omentum. Scale bars, 5 mm. *n* = 4; data represent one of three independent experiments. All data are represented as mean ± SEM. In (A), (D), (E), and (G)–(K), we used an unpaired t test. In (B) and (C), we used two-way ANOVA followed by Sidák's multiple-comparisons test.

SUPPLEMENTAL INFORMATION

Supplemental information can be found online at <https://doi.org/10.1016/j.celrep.2024.114096>.

ACKNOWLEDGMENTS

This work was supported by AIRC IG 21635 (to F.B.). S.J., L.L., and L.G.M. were supported by ICGEB pre- or post-doctoral fellowships. R.A. is supported by Italian Telethon. We thank Giulia Canarutto and Silvano Piazza (ICGEB Trieste) for the initial RNA-seq data processing. We also extend our gratitude to Dr. M. Ruhland and Prof. M. Krummel for providing reporter plasmids for ZsGreen and OVA and Dr. María Casanova-Acebes (CNIO, Madrid) for insightful discussions on the project. The graphical abstract and some schematic representations were created using BioRender.

AUTHOR CONTRIBUTIONS

F.B. and S.J. conceived the study. F.B. supervised the planning and execution of experiments. S.J. performed experiments and data analysis. L.L., L.G.M., G.M.P., and R.A. assisted in the execution of experiments, figure preparation, and critical discussion of the data. L.G.M. also curated biostatistics. M.B. and I.P.O. assisted in execution of experiments. M.P. and M.G. prepared lipid particles for PS targeting. D.V. provided DAAM particles and the methodology for conjugation and assisted in critical discussion of the data obtained using DAAMps.

DECLARATION OF INTERESTS

The authors declare no competing interests.

Received: September 14, 2023

Revised: February 20, 2024

Accepted: March 27, 2024

Published: April 11, 2024

REFERENCES

1. Cassetta, L., and Pollard, J.W. (2018). Targeting macrophages: therapeutic approaches in cancer. *Nat. Rev. Drug Discov.* *17*, 887–904. <https://doi.org/10.1038/nrd.2018.169>.
2. DeNardo, D.G., and Ruffell, B. (2019). Macrophages as regulators of tumour immunity and immunotherapy. *Nat. Rev. Immunol.* *19*, 369–382. <https://doi.org/10.1038/s41577-019-0127-6>.
3. Jahchan, N.S., Mujal, A.M., Pollack, J.L., Binnewies, M., Sriram, V., Reyno, L., and Krummel, M.F. (2019). Tuning the Tumor Myeloid Microenvironment to Fight Cancer. *Front. Immunol.* *10*, 1611. <https://doi.org/10.3389/fimmu.2019.01611>.
4. Pan, Y., Yu, Y., Wang, X., and Zhang, T. (2020). Tumor-Associated Macrophages in Tumor Immunity. *Front. Immunol.* *11*, 583084. <https://doi.org/10.3389/fimmu.2020.583084>.
5. Allavena, P., Sica, A., Garlanda, C., and Mantovani, A. (2008). The Yin-Yang of tumor-associated macrophages in neoplastic progression and immune surveillance. *Immunol. Rev.* *222*, 155–161. <https://doi.org/10.1111/j.1600-065X.2008.00607.x>.
6. Casanova-Acebes, M., Dalla, E., Leader, A.M., LeBerichel, J., Nikolic, J., Morales, B.M., Brown, M., Chang, C., Troncoso, L., Chen, S.T., et al. (2021). Tissue-resident macrophages provide a pro-tumorigenic niche to early NSCLC cells. *Nature* *595*, 578–584. <https://doi.org/10.1038/s41586-021-03651-8>.
7. Etzerodt, A., Moulin, M., Doktor, T.K., Delfini, M., Mossadegh-Keller, N., Bajenoff, M., Sieweke, M.H., Moestrup, S.K., Auphan-Anezin, N., and Lawrence, T. (2020). Tissue-resident macrophages in omentum promote metastatic spread of ovarian cancer. *J. Exp. Med.* *217*, e20191869. <https://doi.org/10.1084/jem.20191869>.

8. Nalio Ramos, R., Missolo-Koussou, Y., Gerber-Ferder, Y., Bromley, C.P., Bugatti, M., Núñez, N.G., Tosello Boari, J., Richer, W., Menger, L., Denizeau, J., et al. (2022). Tissue-resident FOLR2+ macrophages associate with CD8+ T cell infiltration in human breast cancer. *Cell* *185*, 1189–1207.e25. <https://doi.org/10.1016/j.cell.2022.02.021>.
9. Bugatti, M., Bergamini, M., Missale, F., Monti, M., Ardiglieri, L., Pezzali, I., Picinoli, S., Caronni, N., Missolo-Koussou, Y., Helft, J., et al. (2022). A Population of TIM4+FOLR2+ Macrophages Localized in Tertiary Lymphoid Structures Correlates to an Active Immune Infiltrate Across Several Cancer Types. *Cancer Immunol. Res.* *10*, 1340–1353. <https://doi.org/10.1158/2326-6066.CIR-22-0271>.
10. Murphy, T.L., and Murphy, K.M. (2022). Dendritic cells in cancer immunology. *Cell. Mol. Immunol.* *19*, 3–13. <https://doi.org/10.1038/s41423-021-00741-5>.
11. Wculek, S.K., Cueto, F.J., Mujal, A.M., Melero, I., Krummel, M.F., and Sanchó, D. (2020). Dendritic cells in cancer immunology and immunotherapy. *Nat. Rev. Immunol.* *20*, 7–24. <https://doi.org/10.1038/s41577-019-0210-z>.
12. Broz, M.L., Binnewies, M., Boldajipour, B., Nelson, A.E., Pollack, J.L., Erle, D.J., Barczak, A., Rosenblum, M.D., Daud, A., Barber, D.L., et al. (2014). Dissecting the tumor myeloid compartment reveals rare activating antigen-presenting cells critical for T cell immunity. *Cancer Cell* *26*, 638–652. <https://doi.org/10.1016/j.ccell.2014.09.007>.
13. Modak, M., Mattes, A.-K., Reiss, D., Skronska-Wasek, W., Langlois, R., Sabarth, N., Konopitzky, R., Ramirez, F., Lehr, K., Mayr, T., et al. (2022). CD206+ tumor-associated macrophages cross-present tumor antigen and drive antitumor immunity. *JCI insight* *7*, e155022. <https://doi.org/10.1172/jci.insight.155022>.
14. Muntjewerff, E.M., Meesters, L.D., and van den Bogaart, G. (2020). Antigen Cross-Presentation by Macrophages. *Front. Immunol.* *11*, 1276. <https://doi.org/10.3389/fimmu.2020.01276>.
15. Kersten, K., Hu, K.H., Combes, A.J., Samad, B., Harwin, T., Ray, A., Rao, A.A., Cai, E., Marchuk, K., Artchoker, J., et al. (2022). Spatiotemporal co-dependency between macrophages and exhausted CD8(+) T cells in cancer. *Cancer Cell* *40*, 624–638.e9. <https://doi.org/10.1016/j.ccell.2022.05.004>.
16. Nixon, B.G., Kuo, F., Ji, L., Liu, M., Capistrano, K., Do, M., Franklin, R.A., Wu, X., Kansler, E.R., Srivastava, R.M., et al. (2022). Tumor-associated macrophages expressing the transcription factor IRF8 promote T cell exhaustion in cancer. *Immunity* *55*, 2044–2058.e5. <https://doi.org/10.1016/j.immuni.2022.10.002>.
17. Ghosn, E.E.B., Cassado, A.A., Govoni, G.R., Fukuhara, T., Yang, Y., Monack, D.M., Bortolucci, K.R., Almeida, S.R., Herzenberg, L.A., and Herzenberg, L.A. (2010). Two physically, functionally, and developmentally distinct peritoneal macrophage subsets. *Proc. Natl. Acad. Sci. USA* *107*, 2568–2573. <https://doi.org/10.1073/pnas.0915000107>.
18. Yona, S., Kim, K.-W., Wolf, Y., Mildner, A., Varol, D., Breker, M., Strauss-Ayali, D., Viukov, S., Guillemins, M., Misharin, A., et al. (2013). Fate mapping reveals origins and dynamics of monocytes and tissue macrophages under homeostasis. *Immunity* *38*, 79–91. <https://doi.org/10.1016/j.immuni.2012.12.001>.
19. Bain, C.C., Hawley, C.A., Garner, H., Scott, C.L., Schridde, A., Steers, N.J., Mack, M., Joshi, A., Guillemins, M., Mowat, A.M.I., et al. (2016). Long-lived self-renewing bone marrow-derived macrophages displace embryo-derived cells to inhabit adult serous cavities. *Nat. Commun.* *7*, ncomms11852. <https://doi.org/10.1038/ncomms11852>.
20. Casanova-Acebes, M., Menéndez-Gutiérrez, M.P., Porcuna, J., Álvarez-Errico, D., Lavin, Y., García, A., Kobayashi, S., Le Berichel, J., Núñez, V., Were, F., et al. (2020). RXRs control serous macrophage neonatal expansion and identity and contribute to ovarian cancer progression. *Nat. Commun.* *11*, 1655. <https://doi.org/10.1038/s41467-020-15371-0>.
21. Weiss, J.M., Davies, L.C., Karwan, M., Ileva, L., Ozaki, M.K., Cheng, R.Y., Ridnour, L.A., Annunziata, C.M., Wink, D.A., and McVicar, D.W. (2018). Itaconic acid mediates crosstalk between macrophage metabolism and

- peritoneal tumors. *J. Clin. Invest.* 128, 3794–3805. <https://doi.org/10.1172/JCI99169>.
22. Xia, H., Li, S., Li, X., Wang, W., Bian, Y., Wei, S., Grove, S., Wang, W., Vatan, L., Liu, J.R., et al. (2020). Autophagic adaptation to oxidative stress alters peritoneal residential macrophage survival and ovarian cancer metastasis. *JCI Insight* 5, e141115. <https://doi.org/10.1172/JCI.INSIGHT.141115>.
 23. Rodriguez-Manzanet, R., Sanjuan, M.A., Wu, H.Y., Quintana, F.J., Xiao, S., Anderson, A.C., Weiner, H.L., Green, D.R., and Kuchroo, V.K. (2010). T and B cell hyperactivity and autoimmunity associated with niche-specific defects in apoptotic body clearance in TIM-4-deficient mice. *Proc. Natl. Acad. Sci. USA* 107, 8706–8711. <https://doi.org/10.1073/pnas.0910359107>.
 24. Roberts, A.W., Lee, B.L., Deguine, J., John, S., Shlomchik, M.J., and Barton, G.M. (2017). Tissue-Resident Macrophages Are Locally Programmed for Silent Clearance of Apoptotic Cells. *Immunity* 47, 913–927.e6. <https://doi.org/10.1016/j.immuni.2017.10.006>.
 25. Wang, Y., Wang, Y., Ding, L., Ren, X., Wang, B., Wang, L., Zhao, S., Yue, X., Wu, Z., Li, C., et al. (2022). Tim-4 reprograms cholesterol metabolism to suppress antiviral innate immunity by disturbing the Insig1-SCAP interaction in macrophages. *Cell Rep.* 41, 111738. <https://doi.org/10.1016/j.celrep.2022.111738>.
 26. Magalhaes, M.S., Smith, P., Portman, J.R., Jackson-Jones, L.H., Bain, C.C., Ramachandran, P., Michailidou, Z., Stimson, R.H., Dweck, M.R., Denby, L., et al. (2021). Role of Tim4 in the regulation of ABCA1+ adipose tissue macrophages and post-prandial cholesterol levels. *Nat. Commun.* 12, 4434. <https://doi.org/10.1038/s41467-021-24684-7>.
 27. Chow, A., Schad, S., Green, M.D., Hellmann, M.D., Allaj, V., Ceglia, N., Zago, G., Shah, N.S., Sharma, S.K., Mattar, M., et al. (2021). Tim-4+ cavity-resident macrophages impair anti-tumor CD8+ T cell immunity. *Cancer Cell* 39, 973–988.e9. <https://doi.org/10.1016/j.ccell.2021.05.006>.
 28. Baghdadi, M., Yoneda, A., Yamashina, T., Nagao, H., Komohara, Y., Nagai, S., Akiba, H., Foretz, M., Yoshiyama, H., Kinoshita, I., et al. (2013). TIM-4 Glycoprotein-Mediated Degradation of Dying Tumor Cells by Autophagy Leads to Reduced Antigen Presentation and Increased Immune Tolerance. *Immunity* 39, 1070–1081. <https://doi.org/10.1016/j.immuni.2013.09.014>.
 29. Caronni, N., Piperno, G.M., Simoncello, F., Romano, O., Vodret, S., Yanagihashi, Y., Dress, R., Dutertre, C.-A., Bugatti, M., Bourdeley, P., et al. (2021). TIM4 expression by dendritic cells mediates uptake of tumor-associated antigens and anti-tumor responses. *Nat. Commun.* 12, 2237. <https://doi.org/10.1038/s41467-021-22535-z>.
 30. Charles, K.A., Kulbe, H., Soper, R., Escorcio-Correia, M., Lawrence, T., Schultheis, A., Chakravarty, P., Thompson, R.G., Kollias, G., Smyth, J.F., et al. (2009). The tumor-promoting actions of TNF-alpha involve TNFR1 and IL-17 in ovarian cancer in mice and humans. *J. Clin. Invest.* 119, 3011–3023. <https://doi.org/10.1172/JCI39065>.
 31. Ruhland, M.K., Roberts, E.W., Cai, E., Mujal, A.M., Marchuk, K., Beppler, C., Nam, D., Serwas, N.K., Binnewies, M., and Krummel, M.F. (2020). Visualizing Synaptic Transfer of Tumor Antigens among Dendritic Cells. *Cancer Cell* 37, 786–799.e5. <https://doi.org/10.1016/j.ccell.2020.05.002>.
 32. Goossens, P., Rodriguez-Vita, J., Etzerodt, A., Masse, M., Rastoin, O., Gouirand, V., Ulas, T., Papantonopoulou, O., Van Eck, M., Auphan-Anezin, N., et al. (2019). Membrane Cholesterol Efflux Drives Tumor-Associated Macrophage Reprogramming and Tumor Progression. *Cell Metab.* 29, 1376–1389.e4. <https://doi.org/10.1016/j.cmet.2019.02.016>.
 33. Miyanishi, M., Segawa, K., and Nagata, S. (2012). Synergistic effect of Tim4 and MFG-E8 null mutations on the development of autoimmunity. *Int. Immunol.* 24, 551–559. <https://doi.org/10.1093/intimm/dxs064>.
 34. Flannagan, R.S., Canton, J., Furuya, W., Glogauer, M., and Grinstein, S. (2014). The phosphatidylserine receptor TIM4 utilizes integrins as coreceptors to effect phagocytosis. *Mol. Biol. Cell* 25, 1511–1522. <https://doi.org/10.1091/mbc.E13-04-0212>.
 35. Mazaheri, F., Breus, O., Durdu, S., Haas, P., Wittbrodt, J., Gilmour, D., and Peri, F. (2014). Distinct roles for BAI1 and TIM-4 in the engulfment of dying neurons by microglia. *Nat. Commun.* 5, 4046–4111. <https://doi.org/10.1038/ncomms5046>.
 36. Schlam, D., Bagshaw, R.D., Freeman, S.A., Collins, R.F., Pawson, T., Fair, G.D., and Grinstein, S. (2015). Phosphoinositide 3-kinase enables phagocytosis of large particles by terminating actin assembly through Rac/Cdc42 GTPase-activating proteins. *Nat. Commun.* 6, 8623. <https://doi.org/10.1038/ncomms9623>.
 37. Vorselen, D., Wang, Y., de Jesus, M.M., Shah, P.K., Footer, M.J., Huse, M., Cai, W., and Theriot, J.A. (2020). Microparticle traction force microscopy reveals subcellular force exertion patterns in immune cell-target interactions. *Nat. Commun.* 11, 20. <https://doi.org/10.1038/s41467-019-13804-z>.
 38. Vorselen, D., Kamber, R.A., Labitigan, R.L.D., Loon, A.P.V., Peterman, E., Delgado, M.K., Lin, S., Rasmussen, J.P., Bassik, M.C., and Theriot, J.A. (2022). Cell Surface Receptors TREM2, CD14 and Integrin α M β 2 Drive Sinking Engulfment in Phosphatidylserine-Mediated Phagocytosis, pp. 1–40.
 39. Savina, A., Jancic, C., Hugues, S., Guermonprez, P., Vargas, P., Moura, I.C., Lennon-Duménil, A.M., Seabra, M.C., Raposo, G., and Amigorena, S. (2006). NOX2 Controls Phagosomal pH to Regulate Antigen Processing during Crosspresentation by Dendritic Cells. *Cell* 126, 205–218. <https://doi.org/10.1016/J.CELL.2006.05.035>.
 40. Savina, A., Peres, A., Cebrian, I., Carmo, N., Moita, C., Hacohen, N., Moita, L.F., and Amigorena, S. (2009). The small GTPase Rac2 controls phagosomal alkalization and antigen crosspresentation selectively in CD8(+) dendritic cells. *Immunity* 30, 544–555. <https://doi.org/10.1016/j.immuni.2009.01.013>.
 41. Canton, J., Blees, H., Henry, C.M., Buck, M.D., Schulz, O., Rogers, N.C., Childs, E., Zelenay, S., Rhys, H., Domart, M.-C., et al. (2021). The receptor DNGR-1 signals for phagosomal rupture to promote cross-presentation of dead-cell-associated antigens. *Nat. Immunol.* 22, 140–153. <https://doi.org/10.1038/s41590-020-00824-x>.
 42. Krishnan, V., Tallapragada, S., Schaar, B., Kamat, K., Chanana, A.M., Zhang, Y., Patel, S., Parkash, V., Rinker-Schaeffer, C., Folkens, A.K., et al. (2020). Omental macrophages secrete chemokine ligands that promote ovarian cancer colonization of the omentum via CCR1. *Commun. Biol.* 3, 1–13. <https://doi.org/10.1038/s42003-020-01246-z>.
 43. Xia, H., Li, S., Li, X., Wang, W., Bian, Y., Wei, S., Grove, S., Wang, W., Vatan, L., Liu, J.R., et al. (2020). Autophagic adaptation to oxidative stress alters peritoneal residential macrophage survival and ovarian cancer metastasis. *JCI insight* 5, e141115. <https://doi.org/10.1172/jci.insight.141115>.
 44. Louwe, P.A., Badiola Gomez, L., Webster, H., Perona-Wright, G., Bain, C.C., Forbes, S.J., and Jenkins, S.J. (2021). Recruited macrophages that colonize the post-inflammatory peritoneal niche convert into functionally divergent resident cells. *Nat. Commun.* 12, 1770. <https://doi.org/10.1038/s41467-021-21778-0>.
 45. Weiss, J.M., Davies, L.C., Karwan, M., Ileva, L., Ozaki, M.K., Cheng, R.Y., Ridnour, L.A., Annunziata, C.M., Wink, D.A., and McVicar, D.W. (2018). Itaconic acid mediates crosstalk between macrophage metabolism and peritoneal tumors. *J. Clin. Invest.* 128, 3794–3805. <https://doi.org/10.1172/JCI99169>.
 46. Okabe, Y., and Medzhitov, R. (2014). Tissue-specific signals control reversible program of localization and functional polarization of macrophages. *Cell* 157, 832–844. <https://doi.org/10.1016/j.cell.2014.04.016>.
 47. Park, M.D., Reyes-Torres, I., LeBerichel, J., Hamon, P., LaMarche, N.M., Hegde, S., Belabed, M., Troncoso, L., Grout, J.A., Magen, A., et al. (2023). TREM2 macrophages drive NK cell paucity and dysfunction in lung cancer. *Nat. Immunol.* 24, 792–801. <https://doi.org/10.1038/s41590-023-01475-4>.
 48. Tseng, D., Volkmer, J.-P., Willingham, S.B., Contreras-Trujillo, H., Fathman, J.W., Fernhoff, N.B., Seita, J., Inlay, M.A., Weiskopf, K., Miyanishi, M., and Weissman, I.L. (2013). Anti-CD47 antibody-mediated

- phagocytosis of cancer by macrophages primes an effective antitumor T-cell response. *Proc. Natl. Acad. Sci. USA* 110, 11103–11108. <https://doi.org/10.1073/pnas.1305569110>.
49. Enders, M., Franken, L., Philipp, M.-S., Kessler, N., Baumgart, A.-K., Eichler, M., Wiertz, E.J.H., Garbi, N., and Kurts, C. (2020). Splenic Red Pulp Macrophages Cross-Prime Early Effector CTL That Provide Rapid Defense against Viral Infections. *J. Immunol.* 204, 87–100. <https://doi.org/10.4049/jimmunol.1900021>.
 50. Mauvais, F.-X., and van Endert, P. (2023). Cross-presentation by the others. *Semin. Immunol.* 67, 101764. <https://doi.org/10.1016/j.smim.2023.101764>.
 51. den Haan, J.M., Lehar, S.M., and Bevan, M.J. (2000). CD8(+) but not CD8(-) dendritic cells cross-prime cytotoxic T cells in vivo. *J. Exp. Med.* 192, 1685–1696. <https://doi.org/10.1084/jem.192.12.1685>.
 52. Leibundgut-Landmann, S., Osorio, F., Brown, G.D., and Reis e Sousa, C. (2008). Stimulation of dendritic cells via the dectin-1/Syk pathway allows priming of cytotoxic T-cell responses. *Blood* 112, 4971–4980. <https://doi.org/10.1182/blood-2008-05-158469>.
 53. Nakayama, M., Akiba, H., Takeda, K., Kojima, Y., Hashiguchi, M., Azuma, M., Yagita, H., and Okumura, K. (2009). Tim-3 mediates phagocytosis of apoptotic cells and cross-presentation. *Blood* 113, 3821–3830. <https://doi.org/10.1182/blood-2008-10-185884>.
 54. Schulz, O., and Reis e Sousa, C. (2002). Cross-presentation of cell-associated antigens by CD8alpha+ dendritic cells is attributable to their ability to internalize dead cells. *Immunology* 107, 183–189. <https://doi.org/10.1046/j.1365-2567.2002.01513.x>.
 55. Subramanian, M., Hayes, C.D., Thome, J.J., Thorp, E., Matsushima, G.K., Herz, J., Farber, D.L., Liu, K., Lakshmana, M., and Tabas, I. (2014). An AXL/LRP-1/RANBP9 complex mediates DC efferocytosis and antigen cross-presentation in vivo. *J. Clin. Invest.* 124, 1296–1308. <https://doi.org/10.1172/JCI72051>.
 56. Rodríguez-Silvestre, P., Laub, M., Krawczyk, P.A., Davies, A.K., Schessner, J.P., Parveen, R., Tuck, B.J., McEwan, W.A., Borner, G.H.H., and Kozik, P. (2023). Perforin-2 is a pore-forming effector of endocytic escape in cross-presenting dendritic cells. *Science* 380, 1258–1265. <https://doi.org/10.1126/science.adg8802>.
 57. Theisen, D.J., Davidson, J.T., 4th, Briseño, C.G., Gargaro, M., Lauron, E.J., Wang, Q., Desai, P., Durai, V., Bagadia, P., Brickner, J.R., et al. (2018). WDFY4 is required for cross-presentation in response to viral and tumor antigens. *Science* 362, 694–699. <https://doi.org/10.1126/science.aat5030>.
 58. van Endert, P. (2016). Intracellular recycling and cross-presentation by MHC class I molecules. *Immunol. Rev.* 272, 80–96. <https://doi.org/10.1111/immr.12424>.
 59. Liebl, D., and Griffiths, G. (2009). Transient assembly of F-actin by phagosomes delays phagosome fusion with lysosomes in cargo-overloaded macrophages. *J. Cell Sci.* 122, 2935–2945. <https://doi.org/10.1242/jcs.048355>.
 60. Yu, Y., Zhang, Z., and Yu, Y. (2023). Timing of Phagosome Maturation Depends on Their Transport Switching from Actin to Microtubule Tracks. *J. Phys. Chem. B* 127, 9312–9322. <https://doi.org/10.1021/acs.jpcc.3c05647>.
 61. Poirier, M.B., Fiorino, C., Rajasekar, T.K., and Harrison, R.E. (2020). F-actin flashes on phagosomes mechanically deform contents for efficient digestion in macrophages. *J. Cell Sci.* 133, jcs239384. <https://doi.org/10.1242/jcs.239384>.
 62. Moon, B., Lee, J., Lee, S.A., Min, C., Moon, H., Kim, D., Yang, S., Moon, H., Jeon, J., Joo, Y.E., and Park, D. (2020). Mertk Interacts with Tim-4 to Enhance Tim-4-Mediated Efferocytosis. *Cells* 9, 1625–1711. <https://doi.org/10.3390/cells9071625>.
 63. Lee, J., Park, B., Moon, B., Park, J., Moon, H., Kim, K., Lee, S.-A., Kim, D., Min, C., Lee, D.-H., et al. (2019). A scaffold for signaling of Tim-4-mediated efferocytosis is formed by fibronectin. *Cell Death Differ.* 26, 1646–1655. <https://doi.org/10.1038/s41418-018-0238-9>.
 64. Toda, S., Hanayama, R., and Nagata, S. (2012). Two-step engulfment of apoptotic cells. *Mol. Cell Biol.* 32, 118–125. <https://doi.org/10.1128/MCB.05993-11>.
 65. Cieniewicz, B., Bhatta, A., Torabi, D., Baichoo, P., Saxton, M., Arballo, A., Nguyen, L., Thomas, S., Kethar, H., Kukutla, P., et al. (2023). Chimeric TIM-4 receptor-modified T cells targeting phosphatidylserine mediates both cytotoxic anti-tumor responses and phagocytic uptake of tumor-associated antigen for T cell cross-presentation. *Mol. Ther.* 37, 2132–2153. <https://doi.org/10.1016/j.ymthe.2023.05.009>.
 66. Dingjan, I., Verboogen, D.R., Paardekooper, L.M., Revelo, N.H., Sittig, S.P., Visser, L.J., Mollard, G.F.v., Henriët, S.S., Figdor, C.G., Ter Beest, M., and van den Bogaart, G. (2016). Lipid peroxidation causes endosomal antigen release for cross-presentation. *Sci. Rep.* 6, 22064. <https://doi.org/10.1038/srep22064>.
 67. Cunha, L.D., Yang, M., Carter, R., Guy, C., Harris, L., Crawford, J.C., Quarto, G., Boada-Romero, E., Kalkavan, H., Johnson, M.D.L., et al. (2018). LC3-Associated Phagocytosis in Myeloid Cells Promotes Tumor Immune Tolerance. *Cell* 175, 429–441.e16. <https://doi.org/10.1016/j.cell.2018.08.061>.
 68. Colbert, J.D., Cruz, F.M., and Rock, K.L. (2020). Cross-presentation of exogenous antigens on MHC I molecules. *Curr. Opin. Immunol.* 64, 1–8. <https://doi.org/10.1016/j.coi.2019.12.005>.
 69. Dransfield, I., Zagórska, A., Lew, E.D., Michail, K., and Lemke, G. (2015). Mer receptor tyrosine kinase mediates both tethering and phagocytosis of apoptotic cells. *Cell Death Dis.* 6, 16466–e17110. <https://doi.org/10.1038/cddis.2015.18>.
 70. Calpe-Berdiel, L., Zhao, Y., de Graauw, M., Ye, D., van Santbrink, P.J., Mommaas, A.M., Foks, A., Bot, M., Meurs, I., Kuiper, J., et al. (2012). Macrophage ABCA2 deletion modulates intracellular cholesterol deposition, affects macrophage apoptosis, and decreases early atherosclerosis in LDL receptor knockout mice. *Atherosclerosis* 223, 332–341. <https://doi.org/10.1016/j.atherosclerosis.2012.05.039>.
 71. Piehler, A., Kaminski, W.E., Wenzel, J.J., Langmann, T., and Schmitz, G. (2002). Molecular structure of a novel cholesterol-responsive A subclass ABC transporter, ABCA9. *Biochem. Biophys. Res. Commun.* 295, 408–416. [https://doi.org/10.1016/s0006-291x\(02\)00659-9](https://doi.org/10.1016/s0006-291x(02)00659-9).
 72. Kemp, S.B., Carpenter, E.S., Steele, N.G., Donahue, K.L., Nwosu, Z.C., Pacheco, A., Velez-Delgado, A., Menjivar, R.E., Lima, F., The, S., et al. (2021). Apolipoprotein E Promotes Immune Suppression in Pancreatic Cancer through NF-κB-Mediated Production of CXCL1. *Cancer Res.* 81, 4305–4318. <https://doi.org/10.1158/0008-5472.CAN-20-3929>.
 73. Hayakawa, S., Tamura, A., Nikiforov, N., Koike, H., Kudo, F., Cheng, Y., Miyazaki, T., Kubekina, M., Kirichenko, T.V., Orekhov, A.N., et al. (2022). Activated cholesterol metabolism is integral for innate macrophage responses by amplifying Myd88 signaling. *JCI insight* 7, e138539. <https://doi.org/10.1172/jci.insight.138539>.
 74. Love, M.I., Huber, W., and Anders, S. (2014). Moderated estimation of fold change and dispersion for RNA-seq data with DESeq2. *Genome Biol.* 15, 550. <https://doi.org/10.1186/s13059-014-0550-8>.
 75. Yu, G., Wang, L.-G., Han, Y., and He, Q.-Y. (2012). clusterProfiler: an R package for comparing biological themes among gene clusters. *OMICS* 16, 284–287. <https://doi.org/10.1089/omi.2011.0118>.
 76. Maxson, M.E., Abbas, Y.M., Wu, J.Z., Plumb, J.D., Grinstein, S., and Rubinstein, J.L. (2022). Detection and quantification of the vacuolar H⁺-ATPase using the Legionella effector protein SidK. *J. Cell Biol.* 221, e202107174. <https://doi.org/10.1083/jcb.202107174>.
 77. Harel-Adar, T., Ben Mordechai, T., Amsalem, Y., Feinberg, M.S., Leor, J., and Cohen, S. (2011). Modulation of cardiac macrophages by phosphatidylserine-presenting liposomes improves infarct repair. *Proc. Natl. Acad. Sci. USA* 108, 1827–1832. <https://doi.org/10.1073/pnas.1015623108>.

STAR★METHODS

KEY RESOURCES TABLE

REAGENT or RESOURCE	SOURCE	IDENTIFIER
<i>Antibodies</i>		
anti-CD45 APC-fire 750 (clone 30-F11)	BioLegend	Cat#103154 RRID:AB_2572115
anti-NK1.1 FITC (clone PK136)	BioLegend	Cat#108705 RRID:AB_313393
anti-CD19 FITC (clone 6D5)	BioLegend	Cat#115505 RRID:AB_313641
anti-CD19-PE-Cy5 (1D3)	eBioscience	Cat#15-0193-82 RRID:AB_657672
anti-CD45R/B220 FITC (clone RA3-6B2)	BioLegend	Cat#103206 RRID:AB_312991
anti-Ly6G FITC (clone 1A8)	BioLegend	Cat#127605 RRID:AB_1236488
anti-Ly6G PE (clone 1A8)	BioLegend	Cat#127608 RRID:AB_1186104
anti-Ly6C-Alexa Fluor 488 (clone HK1.4)	eBioscience	Cat#53-5932-82 RRID:AB_2574427
anti-Ly6C BV570(clone HK1.4)	BioLegend	Cat#128029 RRID:AB_10896061
anti-CD3 FITC (clone 145-2C11)	BioLegend	Cat#100305 RRID:AB_312671
anti-CD3 PerCP (clone 145-2C11)	BioLegend	Cat#100328 RRID:AB_893320
anti-CD3 Alexa Fluor 700 (clone 17A2)	BioLegend	Cat#100215 RRID:AB_493696
anti-CD4 BV785 (clone GK1.5)	BioLegend	Cat#100453 RRID:AB_2565843
anti-CD8 APC (clone 53-6.7)	BioLegend	Cat#100712 RRID:AB_312750
anti-CD8 BV605 (clone 53-6.7)	BioLegend	Cat#100743 RRID:AB_2561352
anti CD11b APC (clone M1/70)	BioLegend	Cat#101211 RRID:AB_312794
anti-CD11b BV421(clone M1/70)	BD Bioscience	Cat#562605 RRID:AB_11152949
anti-CD11b PerCP-Cy5.5 (clone M1/70)	BioLegend	Cat#101228 RRID:AB_893233
anti-F4/80 Alexa Fluor 488 (clone MCA497)	Bio-Rad	Cat#MCA497A488T RRID:AB_1102554
anti-F4/80 BV421 (clone BM8)	BioLegend	Cat#123131 RRID:AB_2563102
anti-F4/80 PE (clone BM8)	eBioscience	Cat#12-4801-82 RRID:AB_465923
anti-I-A/I-E Alexa Fluor 700 (clone M5/114.15.2)	BioLegend	Cat#107622 RRID:AB_493727
anti-Tim4 Alexa Fluor 647 (clone F31-5G3)	BioLegend	Cat#129907 RRID:AB_1227797
anti-Tim4 PE (clone F31-5G3)	BioLegend	Cat#129905 RRID:AB_1227799

(Continued on next page)

Continued

REAGENT or RESOURCE	SOURCE	IDENTIFIER
anti-IFN γ PE (clone XMG1.2)	BioLegend	Cat#505808 RRID:AB_315401
anti-IFN γ FITC (clone XMG1.2)	BioLegend	Cat#505813 RRID:AB_493312
anti-CD44 PE (clone 1M7)	Biolegend	Cat#103007 RRID:AB_312959
anti-CD62L BV605 (clone MEL-14)	Biolegend	Cat#104453 RRID:AB_2800559
H2K ^b -SIINFEKL (clone 25-D1.16)	Thermo Fisher Scientific	Cat#12-5743-81 RRID:AB_925775
TruStain FCXTM (anti-mouse CD16/32) FC block (93)	BioLegend	Cat#101320 RRID:AB_1574975
anti-HA (clone 3F10)	Roche	Cat#12158167001 RRID:AB_390915
anti-LAMP1 (clone EPR21026)	Abcam	Cat#ab208943 RRID:AB_2923327
anti-ATP6V1A (clone EPR19270)	Abcam	Cat#ab199326 RRID:AB_2802119
anti-EEA1 (Clone C45B10)	Cell Signaling Technology	Cat# #3288 RRID:AB_2096811
anti-Rab6 (clone D37C7)	Cell Signaling Technology	Cat##9625 RRID:AB_10971791
anti-LAMP1 (clone 1D4B)	BD Pharmingen	Cat#553792 RRID:AB_2134499
anti-rabbit Alexa Fluor 555	Thermo Fisher Scientific	Cat#A-21428 RRID:AB_2535849
anti-rat Alexa Fluor 488	Thermo Fisher Scientific	Cat#A-11006 RRID:AB_2534074
anti-rabbit Alexa Fluor 405	Thermo Fisher Scientific	Cat#A-31556 RRID:AB_221605
Mouse IgG	Thermo Fisher Scientific	Cat#02-6502 RRID:AB_2532951
anti-Tim4 (blockade) (clone RMT4-53)	InVivoMab	Cat#BE0171 RRID:AB_2687695
isotype IgG2b, κ (clone LTF2)	Bio X Cell	Cat BE0090 RRID:AB_1107780
Chemicals, peptides, and recombinant proteins		
Collagenase type IV	DBA (Worthington)	Cat#LS004176
LY294,002 hydrochloride	Sigma Aldrich	Cat#L9908-5MG
Diphenyleiiodonium chloride (DPI)	Sigma Aldrich	Cat#D2926-10MG
Bafilomycin A1	Sigma Aldrich	Cat#B1793-10MG
N-[3-Dimethylaminopropyl)- N'-ethylcarbodiimide hydrochloride (EDC)	Sigma Aldrich	Cat#E7750-1G
N-Hydroxysuccinimide (NHS)	Sigma Aldrich	Cat#130672-25G
2-[N-Morpholino]ethane sulfonic acid hydrate (MES)	SIGMA	Cat#M-2933
Ethanolamine	Sigma Aldrich	Cat#398136-25ML
Fluorescein cadaverine	Sigma Aldrich	Cat#92000
Cyanine5-amine	Broadpharm	Cat#BP-22559
DNase I	Sigma (Merck)	Cat#11284932001
SIINFEKL (OVA 257–264)	Invivogen (Aurogene)	Cat#VAC-SIN
Ovalbumin, Fluorescence conjugate (OVA-FITC)	Invitrogen	Cat#O23020

(Continued on next page)

Continued

REAGENT or RESOURCE	SOURCE	IDENTIFIER
DQ™ green BSA	Invitrogen	Cat#D12050
A647 BSA	Invitrogen	Cat#A34785
BSA	SIGMA	Cat#A9576-50ML
EDTA (0.5M), pH 8	Gibco	Cat#A10492-01
Hoechst 33342	Invitrogen	Cat#917368
Paraformaldehyde	Thermo Scientific	Cat#28908
Streptavidin	MedChemExpress	Cat#HY-P3152
Biotin-Phosphatidylserine	Echeleon Biosciences	Cat#31B16
Phosphatidylserine	Avanti Polar Lipids	Cat#P074-25MG
Phosphatidylcholine	Avanti Polar Lipids	Cat#P3556-25MG
ibidi mounting medium	ibidi (Twin helix)	Cat#50001
93-H-2K ^D -SIINFEKL-Pentamer R-PE	Prolmune	Cat#F093-2A-E
CountBright absolute counting beads	Life Technologies	Cat#C36950
rhodamine phalloidin	Thermo-life thecn	Cat#R415
CypHer5E NHS Ester	Cytiva	Cat#PA15401
Trypan Blue solution, 0.4%	Gibco	Cat#15250-061

Critical commercial assays

Fixation/Permeabilization Solution Kit with BD GolgiStop	BD	Cat#554715
SiR-actin kit	Spirochrome	Cat#SC001
RNEasy Micro kit	Qiagen	Cat#74004
mouse IFNg ELISA MAX kit standard set	BioLegend	Cat#430801
APC Annexin V Apoptosis Detection Kit with 7-AAD	BioLegend	Cat#640930
LIVE/DEAD™ Fixable Aqua Dead Cell Stain Kit, for 405nm excitation	Invitrogen	Cat#L34965
CD8 isolation beads	Miltenyi	Cat#130-116-478
Reagents D5000 high sensibility + buffer and ladder for DNA	Agilent Technologies	Cat#5067-5593
SMARTer RNA unique dual index kit 24U - 96 Rxns	Takara (Diatech LabLine)	Cat#634451
SMART-Seq mRNA LP (with UMIs) 24 Rxns	Takara (Diatech LabLine)	Cat#634762
CellTrace™ Violet- Cell Proliferation kit	Invitrogen	Cat#C34557
CFSE Cell Division tracker Kit	BioLegend	Cat#79898
PlasmoTest™ Mycoplasma Detection Kit	Invivogen	Cat#rep-pt1

Deposited data

RNA seq data GEO database	This paper	GSE242989
---------------------------	------------	-----------

Experimental models: Cell lines

ID8	Elena Iacchetti, c/o Mario Colombo lab	Fondazione IRCCS Istituto Nazionale dei Tumori di Milano
ID8-ZsGreen	This paper	N/A
ID8 ^{ZGO}	This paper	N/A
ID8-OVA	This paper	N/A

Experimental models: Organisms/strains

Mouse: C57BL/6	ENVIGO	N/A
Mouse: Tim4 ^{-/-}	Dr S. Nagata, Osaka University	N/A
Mouse: Balb/C	ENVIGO	N/A
Mouse: CD45.1xOT-I	ENVIGO	N/A

(Continued on next page)

Continued

REAGENT or RESOURCE	SOURCE	IDENTIFIER
Oligonucleotides		
pDual-liOva-puroR	David Escors Murugarren, CIB, Navarra	N/A
pSiren-ZsGreen	Dr Megan Ruhland/Dr Matthew Krummel, Oregon Health & Science University/University of California San Francisco, San Francisco, USA	N/A
pCAGGS-Zsgreen-minOVA	Dr Megan Ruhland/Dr Matthew Krummel, Oregon Health & Science University/University of California San Francisco, San Francisco, USA	N/A
Software and algorithms		
Graphpad prism 9 (9.5.1)	GraphPad Software	https://www.graphpad.com/
R (4.1.2)		
GSEA (4.3.2)	Broad institute	https://www.gsea-msigdb.org/gsea/index.jsp
Fiji (2.14.0/1.54f)	National Institutes of Health	https://imagej.net/ij/
Volocity (5.5.1)	Perkin Elmer/Quorum Technologies	https://www.volocity4d.com/about
FACS DiVa	BD Biosciences	
FlowJo (10.8.2)	FlowJo, LLC	https://www.flowjo.com/
Ilastik		https://www.ilastik.org

RESOURCE AVAILABILITY

Lead contact

Further information and requests for resources and reagents should be directed to and will be fulfilled by the lead contact, Federica Benvenuti (benvenuti@icgeb.org). Institutional and funding agency requirements for resource and reagent sharing will be followed.

Materials availability

This study utilized derivatives of ID8 cell lines namely ID8-ZsGreen, ID8^{ZGO} and ID8-OVA that were generated in our lab. This resource is available upon request to the [lead contact](#) as indicated above.

Data and code availability

- Sequencing data have been deposited at GEOdatabase (GEO:GSE242989), which are publicly available as of the 16/09/2023.
- This paper does not report original code.
- Any additional information required to reanalyze the data reported in this paper is available from the [lead contact](#) upon formal request.

EXPERIMENTAL MODEL AND STUDY PARTICIPANT DETAILS

Mouse models

C57BL/6, OT-I (C57BL/6-Tg(TcraTcrb)1100Mjb/J) and Balb/C mice were purchased from Envigo or Jackson Laboratories, respectively. Timd4^{-/-} (Tim4 KO) mice³³ were a kind gift of Professor S. Nagata (Osaka University). Animals were maintained in sterile isolators at the ICGEB animal Bio-experimentation facility (12 h/12 h light and dark cycle, 21°C ± 2°C). Animal care and treatment were conducted with national and international laws and policies (European Economic Community Council Directive 86/609; OJL 358; December 12, 1987). All experiments were performed in accordance with the Federation of European Laboratory Animal Science Association (FELASA) guidelines. The study was approved by International Center for Genetic Engineering and Biotechnology (ICGEB) board for animal welfare and authorized by the Italian Ministry of Health (approval number 459/2022-PR).

Cell lines and cell culture

The ID8 cell line was kindly provided by Elena Lacchetti, c/o Mario Colombo lab, Fondazione IRCCS Istituto Nazionale dei Tumori di Milano. To generate ID8 variants with fluorescent reporters and model antigen, vectors pSiren-ZsGreen and pCAGGS-ZsGreen-min-Ova,³¹ were provided by Dr Megan Ruhland. Briefly, ID8 cells were genetically engineered to stably express ZsGreen using viral transduction with ZsGreen construct. To make ID8^{ZGO} cells, ID8 parental cells were transfected with ZsGreen-minOVA construct and sorted using ARIA II sorter after every 2 passages until stable integrants were obtained. To generate ID8 OVA, ID8 cells were transduced with lentiviral vector pDual-liOva-puroR encoding liOva (kindly provided by David Escors Murugarren, CIB, Navarra).

After puromycin selection, cells were subcloned and single cell clones were tested for HA expression by intracellular staining using anti-HA antibody (clone 3F10, Roche). The parental ID8 cells and the derivatives were maintained in DMEM media supplemented with 4.5 g/mL glucose (Invitrogen) and 10% fetal bovine serum (FBS, Euroclone) and Gentamicin (50 μ g/mL, Gibco) at 37°C in 5% CO₂ and were routinely tested for mycoplasma contamination. Cells were expanded to passage 3 and stored in aliquots in liquid nitrogen. Cells used for *in vivo* challenge have been passed less than five passages.

METHOD DETAILS

Establishment of peritoneal tumors

To track early events of peritoneal tumor establishment at day 15, exponentially growing ID8^{ZGO} or ID8 OVA cells were treated with trypsin (Gibco) and prepared as a single-cell suspension at a concentration of 2×10^7 cells/mL in PBS. WT and Tim4 KO littermates from TIM4 colony were injected intraperitoneally with 100 μ L of the cell suspension (2×10^6 cells). To track post-phagocytic events at 24 h, ID8^{ZGO} or ID8 OVA were exposed to UV-C in a UV cross-linker for 10 min, followed by 3 h incubation at 37°C. Cells were then harvested by scraping and single cell suspension was prepared of density 3×10^6 cells/mL PBS. 100 μ L of this suspension (3×10^5 cells) were injected in WT or Tim4 KO littermates. For all experiments, 100 μ L of PBS was injected as a negative control in a parallel group of control mice. In TIM4 blocking experiments, mice inoculated with ID8^{ZGO} cells were treated with 125 μ g (diluted in PBS) of anti-Tim4 (clone RMT4-53, InVivoMab) or isotype control (rat IgG2b, κ , clone LTF2, InVivoMab) at day -1, and later every 72 h until the experimental endpoint at 15 days. At the experimental endpoint (24 h, 14 or 60 dpi) of each assay, mice were euthanized by cervical dislocation.

H&E of omenta

Omenta were collected from WT and Tim4 KO mice at day 15 after ID8^{ZGO} challenge, stored overnight in 2% formalin at room temperature and later in 50% ethanol in PBS. Tissues were then included in paraffin using standard procedure and sections of 5 μ m thickness were collected. Omental sections were then dewaxed, rehydrated, stained with hematoxylin and counterstained eosin (Bio-Optica, Milano Spa). Ilastik software was trained to automatically detect and segment tumor nodules and the area of tumor nodules was quantified. ImageJ was used to perform measurements and automatic thresholding. % tumor area was calculated as fraction of area of tumor nodules over total area of omentum.

Isolation of murine peritoneal and omental cells

To isolate peritoneal cells from control or tumor bearing mice, 6 mL of ice-cold PBS was injected with syringe in the peritoneal cavity immediately after sacrifice, peritoneal wall was massaged for 2 min and cells were collected by syringe, followed by one wash with PBS and then proceeded for flow cytometry analyses.

Omenta excised from control or ID8^{ZGO} injected animals were mechanically cut into small pieces and digested with Collagenase type 2 (265 U/mL; Worthington) and DNase (250 U/mL; Thermo Scientific) at 37 °C with gentle shaking for 30'. Collagenase action was then stopped by EDTA 10 mM (Invitrogen, Life technologies), and the cell suspension was filtered using 70 μ m cell strainer (Corning). The single cell suspension thus obtained was then processed for flow cytometry analyses.

Flow cytometry

The antibodies used for the experiments are listed in Key resources table and panels used to identify subsets are illustrated in Supplementary Table (S1A, S2A, S3C). Viability was assessed by staining with LIVE/DEAD Fixable Aqua Dead Cell Stain Kit (Invitrogen) Life Technologies). For cell staining, FcR binding sites were blocked by using α CD16/CD32 (Clone 93, Biolegend). Samples were then stained with specific antibodies in 1% BSA in PBS and fixed with 1% PFA in PBS. Production of IFN γ in CD8 T cells isolated from tumor-bearing mice after restimulation was analyzed by intracellular staining of IFN γ in cells fixed and permeabilized using Fixation/Permeabilization solution kit (BD Biosciences) following manufacturer's instructions followed by IFN γ staining. For intracellular staining of OVA-HA, ID8 OVA cells or lung cell suspensions were fixed and permeabilized using Fixation/Permeabilization solution kit (BD Biosciences) following manufacturer's instructions, and then stained with rat monoclonal anti-HA (3F10, Roche) and then with anti-rat A647 (Thermo Fisher).

Absolute cell count was performed by adding CountBright Absolute Counting beads (Invitrogen) to the samples following manufacturer's instructions. After dead cell exclusion and exclusion of cell doublets, the subsequent populations were identified according to the gating strategy provided in Figures S1A, S2A, and S3C. ID8^{ZGO} cells in the peritoneal cavity were identified as CD45⁻ZsGreen⁺.

Phosphatidylserine present on ID8 and derivative cells after UV exposure or after isolation from tumor injected mice at day 15 or in thymocytes after dexamethasone treatment was assessed by Annexin V/7AAD kit (Biolegend).

For sorting specific macrophage subsets, suspension of labeled macrophages was prepared in 2% FBS in PBS, and cells were sorted using FACSria II.

Flow data were acquired with FACS Celesta (BD Biosciences) and analyzed with Diva software (BD Bioscience) or FlowJo software (Tree Star, Inc.).

Induction of apoptosis

To induce apoptosis in ID8 and derivative cells, cells were exposed to UV-C with UV lamp (254 nm, 6W, output 1.7W) for 10 min followed by 4 h incubation in PBS at 37°C. Cells were scraped to detach and prepare a single cell suspension and were stained for AnnexinV/7AAD as described above to analyze induction of apoptosis.

Thymocytes were harvested from Balb/C animals and were incubated with dexamethasone (10 μM) in DMEM +10% FBS medium for 4 h, followed by three washes with DMEM +10% FBS.

Ex vivo priming of OT-I cell by cell sorted macrophages

For *ex vivo* T cell activation assay, LPM, SPM, LPM ZsGreen⁺ or LPM ZsGreen⁻ sorted by flow cytometry from ID8-tumor bearing mice and were plated in U-bottom 96 wells and co-incubated with CTV-labelled OT-I T cells at the ratio 1:2.5 (1x10⁴ macrophages and 2.5 × 10⁴ CD8⁺OTI). After 70 h of co-culture OTI T cell proliferation was assessed by flow cytometry. As positive control, 1x10⁴ sorted LPM were pulsed with class I OVA peptide (SIINFEKL, 90nM) for 2 h. After 2 h stimulation, cells were washed twice in PBS and co-incubated with 2.5x10⁴ OT-I CD8 T cells. Division index was calculated using proliferation platform of FlowJo which is equal to Total Number of Divisions/The number of cells at start of culture. IFN γ production was detected in the supernatant after by ELISA Max Standard sets (Biolegend), following manufacturer's instructions.

Ex vivo phagocytosis and cross-presentation by peritoneal and alveolar macrophages

Peritoneal and alveolar macrophages were sorted from 8-weeks old WT mice according to gating strategy in (Figures S1A, and S3C). 1.5x10⁵ cells were plated in 96-well U-bottom plates in IMDM +10%FBS medium for 2 h. Apoptotic ID8^{ZGO} were then added to at the ratio 1:5 (1.5x10⁴ macrophages and 7.5x10⁴ tumor cells). After 1 h of incubation, cells were washed thrice with PBS to remove non-internalized/non-attached tumor cells and either processed to assess phagocytosis by flow cytometry or co-cultured with CTV-labelled OT-I CD8⁺ T cells in the ratio 1: 2.5 (1.5x10⁴ macrophages to 2.75x10⁴ OT-I T cells). 72 h later, proliferation of OT-I T cells was analyzed by flow cytometry. Division index was calculated using proliferation platform of FlowJo.

Bulk RNA sequencing of ZsGreen+ LPM and analyses

LPM (F4/80^{high} MHCII^{low}) were sorted from naive WT and TIM4 KO mice, whereas, LPM ZsGreen⁺ (F4/80^{high} MHCII^{low} ZsGreen+) were sorted from WT ID8 and TIM4 KO ID8 mice. RNA from sorted cells was extracted using RNeasy micro kit (Qiagen) following manufacturer's instructions. RNA purity, integrity and concentration were determined by NanoDrop (ND-1000 Spectrophotometer, ThermoFisher Scientific) and TapeStation 2200 (Agilent Technologies Inc., Santa Clara, CA, USA). Afterward, 100 ng of total RNA was used to prepare RNA libraries following the instructions of the SMART-Seq^{mRNA} LP, Takara bio kit. Library quality was assessed using TapeStation HS D5000 Screen tape (Agilent) and a narrow distribution with a peak size of approximately 400 bp was observed in all cases. Libraries were quantified by LightCycle qPCR and sequenced in a HiSeqX analyzer (Macrogen) in a run of 2 × 75 cycles and a high output sequencing mode. Approximately twenty million reads were obtained and analyzed for each sample. Fastq files coming from sequencing platform were merged and basic quality controls were performed with FASTQC and PRINSEQ tools. FASTQ files were aligned to the mm10 reference genome, reads were dereplicated for PCR duplicates and gene counts were generated using STAR v.2.5 using quantMode GeneCounts.

Normalization of raw counts followed by differential gene expression analysis was performed with DESeq2⁷⁴ package for R (version 4.1.2). Locally developed scripts were used to format and annotate the differential expression data output from DESeq2. Significant differentially expressed genes were identified as $p < 0.05$, and \log_2 foldchange < 1.5 or > 1.5 . Gene Set Enrichment Analysis (GSEA, Broad Institute) was used to examine enriched pathways. The output of GSEA included an enrichment score (ES), a normalized enrichment score (NES) which accounts for the size of the genes being tested, a p value and an estimated false discovery rate or adjusted p value (p_{adj}). The input for GSEA was prepared by performing pairwise comparisons between DEGs from different populations. Comparative GO analysis was performed with clusterProfiler.⁷⁵ Data are in the process of being deposited in the NCBI's Gene Expression Omnibus database (GSE242989).

Preparation of IgG and PS-functionalized DAAMps

DAAM-particles (6 μm size) synthesized using a membrane-emulsification approach³⁷ were provided by Daan Vorselen. Specifically, a BIS concentration of 2.3% of total acrylic components (100 mg/mL) and a 1.1 μm pore size membrane were used for particles of ~6.2 μm (diameter) and Young's modulus of ~5 kPa and were functionalized as previously described.³⁸ Briefly, DAAM-particles (5% v/v solids) were washed twice with activation buffer (100mM MES pH 6, 200mM NaCl) and resuspended in activation buffer in a volume corresponding to 5% v/v solids. Next, tween 20 (final concentration 0.1% v/v), 1-ethyl-3-(3-dimethylaminopropyl) carbodiimide (EDC) (final concentration 40 mg/mL) and N-hydroxysuccinimide (NHS) (final concentration 20 mg/mL) were added to the particle suspension and incubated for 15 min at room temperature with gentle shaking. Particles were then spun down (16000xg, 2 min), washed thrice with 0.1x PBS, pH 6 supplemented with 0.2% Tween 20 mixing vigorously each time, and resuspended after final wash in equal volume of 0.1X PBS pH 6, 0.2% Tween 20 and 2X PBS, pH 8 (adjusted with NaOH) to make 5% v/v solids suspension of DAAM-particles. Particles were then immediately mixed with protein solutions: For PS-functionalization- streptavidin (final concentration 1 mg/mL, MedChemExpress) and for IgG-functionalization- mouse IgG (final concentration 0.5 mg/mL, Invitrogen) and incubated for 1 h at room temperature with gentle shaking. To visualize the particles in IF based assays, either FITC cadaverine

(0.25 mM, Sigma Aldrich) alone or in combination with cyanine5 amine (0.25mM, BroadPharm) were added for further 30 min. For functionalizing the particles for DQ-BSA based assays, DQ-BSA and Alexa Fluor 647 BSA were added in simultaneously with protein solutions (Streptavidin or IgG) and incubated for 90 min at room temperature with gentle shaking. At the end of incubation with protein and dyes, 100 mM Tris and 100 mM ethanolamine (pH 9) were added to block unreacted NHS groups (30 min at room temperature). DAAM-particles were then spun down (16,000 × g, 2 min) and washed 4× in PBS, pH 7.4 with 0.1% Tween 20. For PS conjugation, Streptavidin-functionalized DAAM-particles were washed in 50% methanol:water (50% MeOH), and resuspended at 10% solids (v/v) in 0.025 mg/mL biotin-phosphatidylserine (Echelon, L-31B16) in 50% MeOH. Finally, DAAM-particles were then washed 3× (10,000 × g, 1 min) with PBS and resuspended in sterile PBS.

Preparation and characterization of PS and PC liposomes

The liposomes were prepared as described⁷⁷ from a lipid mixture (Avanti Polar Lipids) of phosphatidylserine (PS), phosphatidylcholine (PC), and cholesterol (CH) at 1:1:1.33 M ratios, respectively (PS-presenting liposomes), or from PC and CH (1.5:1 M ratio) (PS-lacking liposomes). The degree of PS exposure on liposomes was assessed by (i) binding of FITC-AnnexinV to PS on liposome surface and analysis by FACS and (ii) measuring the zeta potential of liposome preparations using Zeta Plus particle size analyzer (Malvern Panalytical). Liposomes were obtained of size 100 ± 10nm.

To enable detection of liposome uptake by macrophages, the liposomes containing Alexa Fluor 647-Bovine Serum Albumin (BSA) and DQ-Bovine Serum Albumin were prepared. For targeted antigen delivery to LPM and tracking their cross-presentation ability liposomes containing protein OVA were prepared. During hydration of the lipid film, 500 μL equimolar solution of A647-BSA and DQ-BSA solution (1 mg/mL) or FITC-OVA (1 mg/mL) were added to 16 μmol of dried lipid film. To remove unencapsulated protein, liposomes were washed with saline, subjected to dialysis overnight and centrifuged (2500 × g, 15 min, 22°C) three times. The final pellets were resuspended in saline, to yield a final suspension concentration of 33.3 μmol lipid/mL. Encapsulation efficiency was determined by performing protein estimation assay on liposome solution.

Degradation assay (DQ-BSA)

For liposome based assay: WT and Tim4 KO LPM were pulsed for 10 min at 37°C with PS-liposomes or PC-liposomes encapsulating Alexa Fluor 647-BSA and DQ BSA (2 μmol/million cells). For DAAMps based assay: IgG or PS-functionalized DAAMps conjugated with Alexa Fluor 647 BSA and DQ-BSA were added to LPM in the ratio 1: 10 (LPM: DAAMps). Cells were washed 4X with cold PBS in order to remove nonspecific binding/non-internalised liposomes/DAAMps from the cell surface. Cells were then acquired on FACS Celesta, BD for 90 min at every 5 min interval at 37°C and median fluorescent intensity of DQ-BSA normalized on Alexa Fluor 647-BSA⁺ cells was recorded. DQ-BSA degradation index was calculated as log fold change of median fluorescent intensity of DQ-BSA on Alexa Fluor 647⁺ F4/80^{high} macrophages over median fluorescent intensity of DQ-BSA on F4/80^{high} macrophages at time 0 min.

Tracking the rate of lysosomal acidification using cypHer labeled thymocytes

LPM were isolated from peritoneal lavage with ice-cold PBS from naive, WT mice and allowed to adhere in μ-slide chambered coverslips (ibidi) for 6 h. Thymocytes were isolated from Balb/C mouse and were incubated with dexamethasone (10 μM) in DMEM +10% FBS for 4 h at 37°C. After 4 h, cells were washed twice with PBS and stained with CTV 5 μM (Invitrogen) and cypHer5E-Alexa Fluor 647 5 μM (Cytiva) in PBS +10% carbonate buffer (pH 9.2) at 37°C for 20'. Unbound dye was quenched by adding complete medium and washing the cells. Peritoneal cells were pulsed with apoptotic, labeled thymocytes for 10' at 37°C and immediately stored on ice, followed by staining with anti-F4/80 for flow cytometry analysis for about 15–20 min at 4°C. Chase was then allowed at 37°C, fractions were collected at indicated time points and immediately fixed with 1% PFA and median fluorescent intensity of cypHer5E Alexa Fluor 647 on CTV⁺ F4/80^{high} macrophages was recorded by flow cytometry. For certain assays, LPM were treated with Bafilomycin A1 (100 nM) or DPI (5 μM) 30 min prior to the pulse with apoptotic thymocytes as well as during chase. Acidification index was quantified as log fold change of median fluorescent intensity of cypHer5E on CTV⁺ F4/80^{high} macrophages at each indicated time over median fluorescent intensity of cypHer5E of F4/80^{high} macrophages at time 0 min.

Confocal imaging of peritoneal macrophages and quantification

LPM were obtained from naive WT or Tim4 KO animals and plated on ibidi chambers in IMDM for 6 h. Where siR-Actin was used to mark Actin, siR Actin (final concentration 200 nM) and Verapamil (final concentration 1 μM) were added during the time of plating. LPM were then pulsed with apoptotic ID8 ZsGreen⁺ for 15 min at 37°C, followed by three washes with cold PBS to remove non-bound thymocytes. After 15, 30 or 45 min of chase at 37°C, cells were fixed with 4% PFA for 5 min at room temperature. Blocking was performed with 5% horse serum followed by staining with indicated antibodies. Nucleus was stained with Hoechst 33342 (Invitrogen) and mounting medium (ibidi) was added to preserve the samples until acquired. Where PI3K-inhibitor LY294002 was used, WT LPM were treated with the inhibitor (final concentration 100 μM) 20 min prior to the pulse with apoptotic cells as well as during the chase. All the steps were performed in ibidi chambers. Confocal images were acquired with an LSM 880 META reverse microscope (Zeiss) with a 63×/1.4 NA plan oil objective. Image analyses were performed using Volocity 3D Image Analysis Software 5.5.1 (PerkinElmer) and Fiji (NIH). Phagocytic index was calculated for each field using the following formula. Phagocytic index= (the number of internalized thymocytes or DAAMps/Total LPM)× (the number of LPM that have internalized thymo or DAAMps/Total number of

LPM)x100. Curvature of actin phagocytic cup was calculated with the Kappa: a Fiji plugin for curvature analysis. To quantify actin surrounding cargo, within each cell (macrophage) we computed annular area of width 0.8 μm around cargo and measured actin integrated density followed by normalization with actin density per cell (macrophage). vATPase around cargo was quantified in 2 μm annular area surrounding the thymocytes. 'Average thymocyte area' was obtained from calculating area of $n > 20$ uninternalized thymocytes. To quantify cargo degradation, scoring was done based on individual cargo area. "Intact": Average thymocyte area $\pm 10\%$, "Partially digested": Between 30 and 90% $\pm 10\%$ of Average thymocyte area, "Completely digested": $<20\% \pm 10\%$ of Average thymocyte area.

Detection of OVA-MHC-I complexes on surface of peritoneal macrophages

To detect specific MHC class-I OVA complexes peritoneal cells from tumor-bearing mice were incubated for 1 h at 37 $^{\circ}\text{C}$ with PE-coupled H2K^b-SIINFEKL mAb (25-D1.16) (BioLegend). Cells were washed and stained with extracellular antibodies to identify LPM and SPM and analyzed by flow cytometry. As negative control, LPM were isolated from control mice. As positive control, LPM and SPM isolated from control mice were stimulated for 2 h with 50nM SIINFEKL and stained as above.

Adoptive transfer of OT-I CD8 T cells and *in vivo* proliferation

CD8 T cells were obtained from lymph nodes of mice expressing congenic marker CD45.1 and OVA-specific TCR chain V β 5 (OT-I). 1×10^6 CD45.1⁺OTI CD8⁺ OVA-specific T cells were labeled with CFSE (5 μM , Biolegend) or CTV (5 μM , Thermo Fisher Scientific), and intraperitoneally injected into WT or Tim4 KO mice. After 16 h, mice were injected with 2×10^5 apoptotic ID8-OVA. For experiments with liposome-mediated antigen delivery, OVA-containing PC or PS liposomes amounting to equal concentrations of OVA (1–2 μM). At indicated times (2 days or 15 days) after tumor or liposomes challenge, and peritoneal ascites were collected, processed as described previously and proliferation was verified by flow cytometry. As a control, total ascites cells were re-stimulated *ex vivo* with OVA class-I peptide SIINFEKL (2 μM).

Activation of endogenous anti-tumor CD8⁺ T responses

For analysis of the activation state of endogenous tumor-infiltrating CD8⁺ T cells in ID8^{ZGO} tumor bearing mice, peritoneal cells were collected at day 14 post-tumor inoculation. Cells were washed with PBS and stimulated with SIINFEKL (2 μM) 37 $^{\circ}\text{C}$ for 4 h in the presence of Golgi Stop (BD Biosciences) to allow accumulation of intracellular cytokines. After viability and surface marker staining, cells were fixed and permeabilized using Cytotfix/Cytoperm solution (BD Biosciences) following manufacturer's instructions, and then stained with anti-IFN γ -PE (XMG1.2, Biolegend).

Tim4 KO mice or WT counterparts were injected with 2×10^6 ID8^{ZGO} cells and sacrificed 14 days post-tumor inoculation. Accumulation of endogenous anti-tumor CD8⁺ T cells in the peritoneal cavity was assessed by using Pro5 MHC H-2Kb Pentamers (Proimmune) following manufacturer's instructions. Briefly, total peritoneal cells were stained with Pro5 MHC H-2Kb Pentamers for 45 min at 4 $^{\circ}\text{C}$, washed and stained to identify CD8 using the gating strategy shown in [Figure S1A](#).

QUANTIFICATION AND STATISTICAL ANALYSIS

All statistical analyses were performed using GraphPad Prism 9 software. All data are presented as the mean \pm SEM, unless otherwise indicated. The number of replicates for each experiment are mentioned in respective figure legends. Statistical significance between two or more groups was evaluated using student's two-tailed t test (paired or unpaired, as applicable), multiple comparisons, one way ANOVA or two-way ANOVA, as appropriate. For acidification and degradation curves, the data were analyzed using non-linear regression by fitting the data into 'one phase association' model ([Figures 5 F, 5H, 5I; and S6D](#)) or 'plateau followed by one phase association' model ([Figure S8G](#)) and plateau values for individual experiments, which were then analyzed by t test or two-way ANOVA as applicable. p values <0.05 were considered significant.